Monthly Notices of the ROYAL ASTRONOMICAL SOCIETY

MNRAS **541,** 1329–1347 (2025) https://doi.org/10.1093/mnras/staf1061
Advance Access publication 2025 July 2

The *JWST* Emission-Line Survey: extending rest-optical narrow-band emission-line selection into the Epoch of Reionization

K. J. Duncan [1]★ D. J. McLeod [1] P. N. Best,[1] C. A. Pirie [1] M. Clausen,[1] R. K. Cochrane [1,2,3] J. S. Dunlop,[1] S. R. Flury,[1] J. E. Geach [4] N. A. Grogin,[5] C. L. Hale [1,6] E. Ibar,[7,8] R. Kondapally,[1,9] Zefeng Li [7] J. Matthee [10] R. J. McLure,[1] Luis Ossa-Fuentes,[7] A. L. Patrick,[1] Ian Smail [9] D. Sobral,[11,12] H. M. O. Stephenson [13] J. P. Stott [13] and A. M. Swinbank [9]

[1]*Institute for Astronomy, University of Edinburgh Royal Observatory, Blackford Hill, Edinburgh EH9 3HJ, UK*
[2]*Department of Astronomy, Columbia University, New York, NY 10027, USA*
[3]*Jodrell Bank Centre for Astrophysics, University of Manchester, Oxford Road, Manchester M13 9PL, UK*
[4]*Centre for Astrophysics Research, School of Physics, Engineering and Computer Science, University of Hertfordshire, Hatfield, AL10 9AB, UK*
[5]*Space Telescope Science Institute, 3700 San Martin Drive, Baltimore, MD 21218, USA*
[6]*Astrophysics, Department of Physics, University of Oxford, Denys Wilkinson Building, Keble Road, Oxford OX1 3RH, UK*
[7]*Instituto de Física y Astronomía, Universidad de Valparaíso, Avda. Gran Bretaña 1111, Valparaíso, Chile*
[8]*Millennium Nucleus for Galaxies (MINGAL)*
[9]*Centre for Extragalactic Astronomy, Department of Physics, Durham University, South Road, Durham DH1 3LE, UK*
[10]*Institute of Science and Technology Austria (ISTA), Am Campus 1, 3400 Klosterneuburg, Austria*
[11]*Departamento de Física, Faculdade de Ciências, Universidade de Lisboa, Edifício C8, Campo Grande, PT1749-016 Lisbon, Portugal*
[12]*BNP Paribas Corporate & Institutional Banking, Torre Ocidente Rua Galileu Galilei, 1500-392 Lisbon, Portugal*
[13]*Department of Physics, Lancaster University, Lancaster LA1 4YB, UK*

Accepted 2025 June 27. Received 2025 June 27; in original form 2024 October 14

ABSTRACT

We present the *JWST* Emission-Line Survey (JELS), a *JWST* imaging programme exploiting the wavelength coverage and sensitivity of the Near-Infrared Camera (NIRCam) to extend narrow-band rest-optical emission-line selection into the Epoch of Reionization (EoR) for the first time, and to enable unique studies of the resolved ionized gas morphology in individual galaxies across cosmic history. The primary JELS observations comprise $\sim 4.7\,\mu$m narrow-band imaging over ~ 63 arcmin^2 designed to enable selection of Hα emitters at $z \sim 6.1$ and a host of novel emission-line samples, including [O III] ($z \sim 8.3$) and Paschen α/β ($z \sim 1.5/2.8$). For the F466N/F470N narrow-band observations, the emission-line sensitivities achieved are up to $\sim 2\times$ more sensitive than current slitless spectroscopy surveys (5σ limits of 0.8–1.2×10^{-18} erg s^{-1}cm^{-2}), corresponding to unobscured Hα star formation rates (SFRs) of 0.9–1.3 $M_\odot$ yr^{-1} at $z \sim 6.1$, extending emission-line selections in the EoR to fainter populations. Simultaneously, JELS also adds F200W broad-band and F212N narrow-band imaging (Hα at $z \sim 2.23$) that probes SFRs $\gtrsim 5\times$ fainter than previous ground-based narrow-band studies ($\sim 0.2\,M_\odot$ yr^{-1}), offering an unprecedented resolved view of star formation at cosmic noon. We present the detailed JELS design, key data processing steps specific to the survey observations, and demonstrate the exceptional data quality and imaging sensitivity achieved. We then summarize the key scientific goals of JELS, demonstrate the precision and accuracy of the expected redshift and measured emission-line recovery through detailed simulations, and present examples of spectroscopically confirmed Hα and [O III] emitters discovered by JELS that illustrate the novel parameter space probed.

Key words: galaxies: evolution – galaxies: high-redshift – surveys – dark ages, reionization, first stars.

1 INTRODUCTION

Since its launch, *JWST* has been delivering on its promise to transform our understanding of the earliest stages of galaxy formation, discovering a wealth of galaxies out to unprecedented redshifts (e.g. Carniani et al. 2024; Robertson et al. 2024), routinely providing spectroscopic confirmation of galaxies at $z > 10$ (e.g. Arrabal Haro et al. 2023; Curtis-Lake et al. 2023) and discovering new populations of active galactic nuclei (AGNs; e.g. Matthee et al. 2023; Labbe et al. 2025), whilst also beginning to reveal the detailed properties of the galaxies that powered the process of cosmic reionization (Sanders et al. 2023; Shapley et al. 2023). These early *JWST* results have demonstrated the potential to begin answering some of the key outstanding questions in extra-galactic astronomy. For example, how and when do the first galaxies assemble? How does the chemical

★ E-mail: kdun@roe.ac.uk

© The Author(s) 2025.
Published by Oxford University Press on behalf of the American Institute of Biological Sciences. This is an Open Access article distributed under the terms of the Creative Commons Attribution License (https://creativecommons.org/licenses/by/4.0/), which permits unrestricted reuse, distribution, and reproduction in any medium, provided the original work is properly cited.

enrichment of the Universe proceed (Arellano-Córdova et al. 2022; Cameron et al. 2023; Curti et al. 2023; Isobe et al. 2023; Topping et al. 2024)? When do the first supermassive black holes (SMBHs) form (Larson et al. 2023a; Greene et al. 2024; Maiolino et al. 2024; Matthee et al. 2024; Labbe et al. 2025)? Which galaxies drive the process of reionization and what is its detailed topology (Tang et al. 2023; Mascia et al. 2024; Umeda et al. 2024; Witstok et al. 2024)?

However, to date, the majority of $z > 6$ galaxy samples confirmed by the *JWST* Near-Infrared Spectrograph (NIRSpec; Jakobsen et al. 2022) have typically been selected on the basis of broad-band colours (de Graaff et al. 2025) or photometric redshift estimates (e.g. Bunker et al. 2024; Hu et al. 2024; Maseda et al. 2024). Such selections, however, can be limited by strong biases, with photometric redshift estimates highly dependent on prior assumptions on the UV continuum slopes and emission-line properties (Arrabal Haro et al. 2023; Larson et al. 2023b). To constrain models of galaxy assembly and understand the processes driving early galaxy evolution (Somerville & Davé 2015; Yung et al. 2019), it is critical to study stellar mass or star formation rate (SFR)-selected samples of galaxies across cosmic time that are as complete and unbiased as possible (and where any remaining biases can be easily modelled).

The increasing strength of optical emission lines at $z > 2$ has been observed extensively (Khostovan et al. 2016; Mármol-Queraltó et al. 2016; Reddy et al. 2018). This trend, along with the ubiquity of high equivalent width emission lines in $z > 5$ galaxies (e.g. De Barros et al. 2019) can therefore be used to our advantage, through the efficient selection of galaxies based on their rest-optical emission lines. Slitless spectroscopic surveys (Kashino et al. 2023; Oesch et al. 2023) have already showcased the scientific potential of emission-line-selected samples with the *JWST*. These surveys provide a powerful method to trace the evolution of star-forming galaxies and AGN throughout cosmic history (Matthee et al. 2023; Meyer et al. 2024; Covelo-Paz et al. 2025).

Complementary to the grism or slitless spectroscopic approach is the selection of emission-line galaxies using photometric narrow-band observations. Like slitless spectroscopy, a key advantage of narrow-band selection is that galaxies are selected on the strength of their emission lines, broadly representing an SFR-selected sample. When compared to broad-band photometric selections, narrow-band surveys also offer the advantage that the robustly selected samples lie within a narrow redshift range while minimizing the complex selection effects and biases (e.g. source blending) of slitless samples. As such, in recent years deep ground-based narrow-band surveys in the optical and near-IR have enabled measurements of the Hα luminosity function (LF) out to $z \sim 2.2$ (Geach et al. 2008; Sobral et al. 2013; Matthee et al. 2017), providing robust measurements of the cosmic SFR density, and enabled detailed studies of the morphology (Sobral et al. 2009, 2016), clustering (Sobral et al. 2010; Geach et al. 2012; Cochrane et al. 2017, 2018) and environment (Sobral et al. 2011) of star-forming galaxies. Finally, narrow-band selections also offer the advantage of providing a direct resolved view of the ionized gas in individual galaxies. Previous narrow-band studies have also provided the samples for high-resolution follow-up observations that enable more detailed morphological, chemical, and dynamical studies (e.g. Swinbank et al. 2012; Stott et al. 2014; Molina et al. 2019; Cheng et al. 2020; Cochrane et al. 2021).

With the inclusion of narrow-band filters on the Near-Infrared Camera (NIRCam; Rieke, Kelly & Horner 2005; Rieke et al. 2023) from 1.645 μm all the way out to 4.7 μm, *JWST* now offers the potential for narrow-band selection of key optical emission lines such as Hα and [O III] out into the Epoch of Reionization (EoR; $z \sim 6.1$ and 8.3, respectively). Simultaneously, the longest wavelength NIRCam narrow-bands can also probe emission lines such as Paα and Paβ that were previously largely inaccessible in galaxies at the peak of cosmic star formation history ($1 \lesssim z \lesssim 3$). The short wavelength (< 2.5 μm) narrow-band filters, while not breaking new redshift ground, can exploit *JWST*'s exceptional resolution and sensitivity to constrain the detailed morphology of ionized gas in galaxies at cosmic noon while also probing substantially fainter populations than previously possible from the ground (e.g. Geach et al. 2008; Sobral et al. 2013; Matthee et al. 2017).

The *JWST* Emission-Line Survey (JELS; GO #2321, PI: Best) is a Cycle 1 NIRCam imaging programme designed to explore this new discovery space using narrow-band observations to detect and study emission-line galaxies across cosmic time. JELS leverages the extraordinary wavelength coverage, spatial resolution, and sensitivity of *JWST*/NIRCam to extend narrow-band galaxy selections into previously inaccessible observational regimes. Specifically, using the F466N/F470N filters at ~ 4.7 μm, the primary goal of JELS is to provide a clean Hα emission-selected sample of galaxies in the EoR ($z = 6.1$) that provides complementary constraints on the cosmic star formation history and whose properties can be characterized and compared against UV-selected samples (Pirie et al. 2025). Simultaneous 2.12 μm (F212N) narrow-band imaging is designed to probe a factor of ~ 5 deeper than previous ground-based studies of Hα at $z \sim 2$ (e.g. Sobral et al. 2013), doing so with sub-kpc resolution to reveal the distribution in star-forming galaxies at the peak of cosmic star formation activity in unprecedented detail. In this paper, we present an overview of JELS; outlining the survey design, the *JWST*/NIRCam observations, the corresponding data-processing and resulting properties of the JELS imaging. We then summarize the broader scientific goals of the survey, with illustrations of the unique statistical and resolved studies it enables. Finally, we demonstrate the practical capabilities of the JELS imaging through realistic simulations of $z > 6$ emission-line galaxy populations, as well as presenting illustrative examples of spectroscopically confirmed Hα and [O III]λ5008 emitters identified by JELS.

The rest of this paper is set out as follows. In Section 2, we present the technical design of the JELS survey, the data reduction process and the photometric properties of the JELS imaging. In Section 3, we outline the scientific goals of JELS and the expected scientific returns. In Section 4, we present detailed simulations of the redshift and emission-line precision that can be achieved by JELS Hα and [O III]λ5008 emission-line selected samples. Section 5 then presents results from a sample of JELS Hα and [O III]λ5008 emission-line candidates confirmed by spectroscopic follow-up observations. Section 6 then summarizes our conclusions. Throughout this paper, all magnitudes are quoted in the AB system (Oke & Gunn 1983) unless otherwise stated. We also assume a ΛCold Dark Matter (ΛCDM) cosmology with $H_0 = 70\,\mathrm{km\,s^{-1}\,Mpc^{-1}}$, $\Omega_m = 0.3$, and $\Omega_\Lambda = 0.7$.

2 SURVEY OVERVIEW

The overall observing strategy and survey design of JELS was driven by requirements of the primary science case: first, to probe sufficient cosmological volume to detect a statistical sample of $z > 6$ Hα emitters (a prediction of 40–60 based on conversion from the UV LF of Bouwens et al. 2015 and assuming UV to Hα conversion as presented in Hao et al. 2011), and secondly to probe significantly below the break of the LF for Hα emitters at $z > 6$, thus identifying 'typical' star-forming galaxies comparable to those selected in Lyman-break selected samples but with a highly complementary selection function.

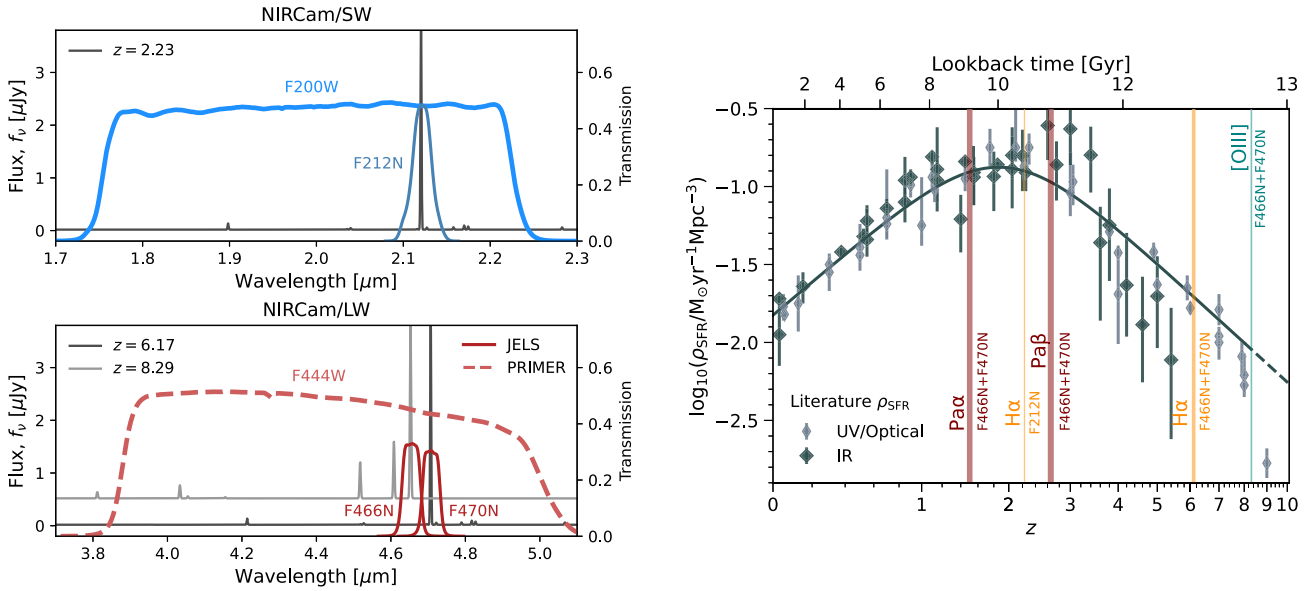

Figure 1. Left: Illustration of the JELS filter-set in the NIRCam/SW (upper panel) and LW bands (lower panel). Shown for reference is an illustrative star-forming galaxy spectral energy distribution redshifted to key redshifts where the narrow-band filters probe Hα ($z = 2.23$ for F212N, $z = 6.17$ for F470N) and [O III]λ5008 ($z = 8.29$ for F466N). The continuum flux density values are normalized arbitrarily for visualization purposes. Right: Key emission lines and SFR-indicators probed by the JELS narrow-band filters in the context of the cosmic SFR density evolution. Literature UV/Optical (narrow diamonds) and infrared (wide diamonds) SFR density measurements are shown from the compilation by Madau & Dickinson (2014, see references therein) and illustrative additional measurements at $z > 3$ from recent studies in the rest-UV (Bouwens et al. 2022) and far-IR (Dudzevičiūtė et al. 2020, for 850 μm sources brighter than > 0.2 mJy).

While designed to be scientifically viable with only existing legacy multiwavelength observations (e.g. CANDELS COSMOS; Grogin et al. 2011; Koekemoer et al. 2011), JELS was designed in tandem with the *JWST* Cycle 1 Guest Observer Treasury Program 'Public Release Imaging For Extragalactic Research' Survey (PRIMER; GO #1837, Dunlop et al. in preparation). The complementary broad-band observations across the full NIRCam wavelength range from PRIMER improve the reliability of narrow-band excess selection at ~ 4.7 μm (see below), and are critical for panchromatic spectral energy distribution modelling and robust emission-line disambiguation for line emitters selected at both 2.12 and ~ 4.7 μm. An additional survey design criterion was therefore for the narrow-band imaging to be located entirely within both the pre-existing deep optical and contemporaneous PRIMER NIRCam observations.

2.1 Survey design

In the NIRCam long-wavelength (LW) channels, JELS employs the closely separated F466N and F470N narrow-band filters, with pivot wavelengths of 4.654 and 4.707 μm, respectively (and effective filter widths, $W_{\rm eff}$, of 0.054 and 0.051 μm). Either through difference imaging between the adjacent F466N/F470N bands, or narrow-band excess selection with respect to the F444W broad-band imaging provided by the PRIMER COSMOS observations, line emitters can be selected in both filters and enable selection of Hα emitters in two overlapping volumes centred at $z \sim 6.09$ and $z \sim 6.17$ (see Fig. 1).

Simultaneously, in the NIRCam short-wavelength (SW) channels, JELS employs the F212N narrow ($\lambda_{\rm pivot} = 2.12$ μm, $W_{\rm eff} = 0.027$ μm) and F200W broad-band ($\lambda_{\rm pivot} = 1.99$ μm, $W_{\rm eff} = 0.419$ μm) filters with a traditional narrow–broad-band approach (Fig. 1). The F212N filter probes Hα at $z = 2.23$, corresponding to the peak epoch of cosmic star formation, significantly extending the luminosity range of existing ground-based studies at this key redshift while also enabling resolved studies of the ionized gas at sub-kpc resolution. Besides ensuring matched broad-band coverage for F212N narrow-band selection, the F200W broad-band imaging also adds 2–3× the PRIMER exposure times within the centre of the field, providing significant gains in sensitivity for broader galaxy evolution studies in this critical legacy field.

JELS uses a 3 × 3 mosaic strategy with 5 per cent overlap in each row and 57 per cent overlap between each column. We also adopt the standard three-point intra-module dithering at each location to fill in short-band intra-chip gaps and account for both bad pixels and cosmic rays, with sub-pixel shifts at each primary dither position. The full JELS mosaic provides contiguous coverage over a total area of ~ 63 arcmin^2. Combining the wavelength coverage of both F466N and F470N, this area corresponds to a Hα selection volume of $\sim 2.4 \times 10^4$ Mpc^3 (at $z \sim 6.1$). For F212N, the single narrower filter results in an approximate Hα selection comoving volume of $\sim 0.9 \times 10^4$ Mpc^3 (at $z \sim 2.2$).

For the NIRCam SW and LW filter pairs, all observations use the MEDIUM-10 read-out strategy, with 6 total integrations/dithers at each mosaic position. The F212N and F470N(+F444W)[1] filter combination was observed with 10 groups per integration, with this observing set-up resulting in an on-sky integration time of 6 313 s over the full mosaic. Over the central ~ 40 per cent of the mosaic that is imaged twice, the total exposure time reaches 12 626 s. The F200W and F466N(+F444W)[1] filter combination was observed with 9 groups per integration with the same number of total integrations and dithers, yielding a total on-sky integration time of 5 669s over

[1]Both F466N and F470N are observed with F444W as a blocking filter. We use '(+ F444W)' here to denote that.

the full mosaic (11 338 s over the central 40 per cent). Note that the difference in groups per integration between F466N and F470N observations (9 versus 10) is a result of changes to the readout strategy from the initial proposal (DEEP-10 to MEDIUM-10) to reduce the impact of cosmic rays, and the additional overheads that resulted in. The F212N/F470N pairing was prioritized to maximize the sensitivity in F212N.

2.2 Observations and image reduction

The initial JELS observations were acquired over the period of 2023 May 6 to May 27. Of these observations, 13 of 18 visits were observed without issue. In five of the eighteen total visits of the JELS observations (one F200W + F466N, four F212N + F470N), the NIRCam imaging was subject to unusually bright scattered light, or 'wisps', that resulted in features in *both* the SW and LW detectors.[2] Initial tests demonstrated that the LW wisps remained spatially invariant within the field of view and have approximately constant amplitude within a visit and could therefore be effectively removed as set out below.

However, unlike most common wisps, the scattered light in the impacted JELS SW images is both extremely bright and shows notable small-scale variation in morphology between exposures within a given visit. With the corresponding LW images also impacted, standard approaches to mitigate the scattered light are not viable (see e.g. Robotham et al. 2023). For the impacted F200W + F466N visit, the availability of the separate PRIMER F200W observations and the limited impact on F466N mean that the overall impact is negligible. However, for the four F212N + F470N visits where the F212N exposures are not viable for the proposed scientific goals, these specific pointings were re-scheduled and successfully observed over the period of 2024 November 23 to November 24.

In the following sections, we describe the current version of the data reduction and the resultant imaging properties from this full data set (v1.0). Other early JELS analyses (Pirie et al. 2025) were based on an earlier data reduction, in which the re-observed frames were not included (v0.8). For completeness, in Appendix A we describe the differences between the v0.8 and v1.0 data sets.

2.2.1 *Imaging pipeline*

To ensure consistency with the key ancillary imaging in the field, all JELS imaging is processed through the Primer Enhanced NIRCam Image Processing Library (PENCIL; Magee et al. in preparation) software, an enhanced version of the *JWST* pipeline (version 1.13.4) and using the JWST_1303.PMAP Calibration Reference Data System (CRDS) file. This PENCIL pipeline includes additional routines for the removal of snowballs and standard wisp artefacts, correction for $1/f$ noise striping as well as background subtraction. The astrometry of the reduced images is tied to the *Gaia* DR3 (Gaia Collaboration 2022) reference frame and stacked to a consistent pixel scale (0.03 arcsec × 0.03 arcsec). Prior to the construction of the final mosaics, we also take additional steps to mitigate the impact of the non-standard wisp artefacts in the five impacted JELS visits.

[2]See e.g. the *JWST* Known Issues: https://jwst-docs.stsci.edu/known-issues-with-jwst-data/nircam-known-issues/nircam-scattered-light-artifacts#NIRCamScatteredLightArtifacts-wisps

2.2.2 *Scattered light removal*

For the affected LW images that drive the primary JELS science aims, subtraction of the wisps is possible, but requires a specific approach tuned to these observations. In NIRCam observations impacted by the typical wisp scattered light patterns, the robust prior positions (and spatial extent) of real sources in the affected SW modules can be obtained from the corresponding unaffected LW module image (Robotham et al. 2023). For the severe wisps in JELS, this is not possible since the LW frames themselves are affected. Templates for the LW scattered light therefore must be derived directly from the observed data and make use of the fact that our observing strategy provides 3 intra-module dithers at each pointing.

The impacted frames are first processed through the initial PENCIL data reduction stages as above. A scattered light template for a given set of exposures is then generated as follows:

(i) Compact sources within the image are identified, with source detection employing a small locally varying background (25 × 25 pixel box-size) to select genuine sources within regions of diffuse scattered light. In each exposure, the compact sources are then masked with additional dilation around each source, consisting of two iterations using a binary dilation structure with connectivity equals one (i.e. no diagonal elements are neighbours).

(ii) The six frames are median stacked in the image plane to produce a wisp template for the frame. The median stacked template is then convolved with a Gaussian smoothing kernel with a full-width at half-maximum (FWHM) of 5 pixels to reduce small-scale noise (with interpolation for any remaining masked pixels).

(iii) A template mask is then generated by smoothing the scattered light template with a larger Gaussian kernel (FWHM = 25 pixels). Regions of the smoothed template image with flux below $0.5 \times \sigma_{\rm RMS}$ are set to zero.

The final step is included to avoid the addition of noise from the generated template to pixels that are largely unaffected by the scattered light. By construction however, this may leave some areas of fainter diffuse scattered light present within individual frames prior to the final mosaicing and combination of all frames covering the region. We mitigate the impact of this low-level scattered light outside the masked regions in the following way. First we mask sources with a dilated segmentation map (size = 5, increasing to size = 20 for the most extended sources). We then make a median stack of the three masked, odd valued dithers and subtracted this from the even valued dithers. The procedure is then applied for subtracting even valued dithers from odd, before the final processed frames were included in the mosaicing. Fig. 2 illustrates the effectiveness of the LW wisp removal on one of the impacted JELS visits.

Due to the extreme brightness and significant exposure-to-exposure variation in the spatial distribution within the affected SW frames, subtraction of the scattered light in SW is not feasible. However, even for the most severely impacted NIRCam SW modules, the majority of pixels in each frame remain perfectly usable for scientific analysis (see right panels of Fig. 2). For the JELS SW data reduction, we therefore follow a similar procedure as above, generating an average scattered light template for each affected module. The scattered light mask generated from template generation procedure outlined above is instead then used to mask the most severe areas of scattered light before the subsequent mosaicing.

Finally, once scattered light has been either subtracted or masked, the JELS imaging is then stacked on to the same 0.03 arcsec pixel grid as the PRIMER COSMOS imaging (see e.g. Donnan et al. 2024) that is tied to the same astrometric reference. In the regions

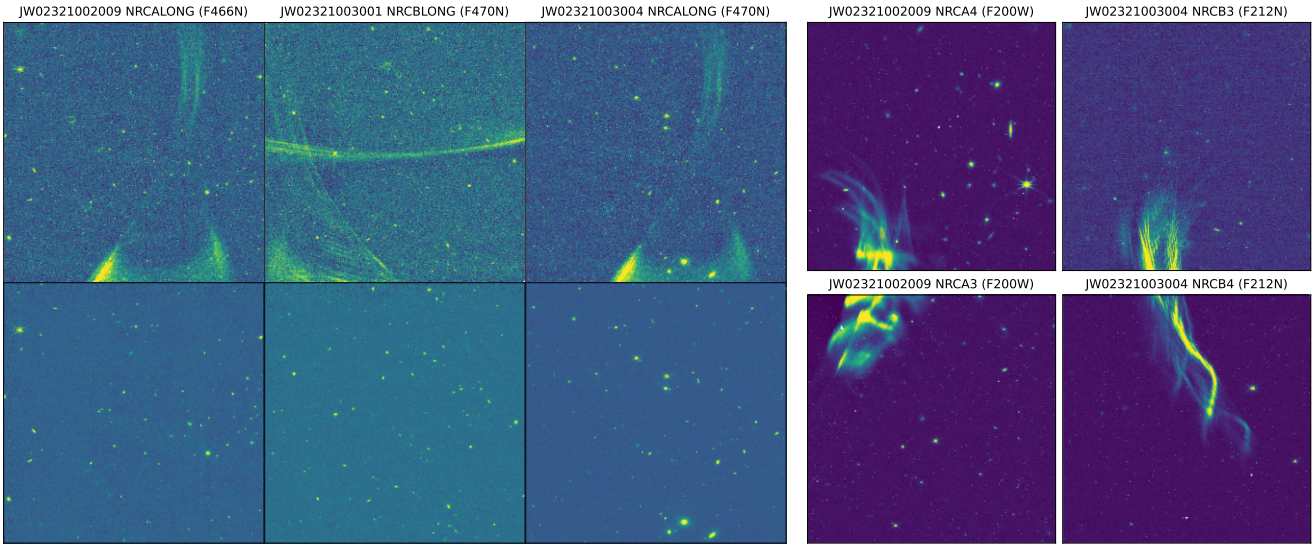

Figure 2. Left: Illustration of the transient scattered light and associated removal for the NIRCam long wavelength imaging. The top row shows reduced individual frames for a single exposure in three of the F466N/F470N visits impacted by scattered light, labelled with the corresponding observation ID, NIRCam module and filter. The bottom row shows the corresponding region of sky from the final mosaic after subtraction of the scattered light in individual frames and all overlapping dithers or mosaic visits have been combined. Each region (i.e. column) is shown with the same colour scale, with a linear stretch between 2 and 99.5 per cent of the individual impacted visit. Right: Illustration of the more extreme scattered light impacting the F200W and F212N observations.

impacted by severe scattered light, the final SW mosaics and the F470N LW mosaic combine both the initial observations (with the severe scattered light treated following the procedure outlined above) and any additional data from the respective repeat observations.

2.3 JELS data properties

Fig. 3 illustrates the relative position of the JELS imaging in the context of the PRIMER COSMOS field for the final observed position angles. With the exception of a small region in the south–west of the field (the majority of which is covered by two or fewer dither positions), the JELS LW narrow-band imaging is fully contained within the NIRCam F444W broad-band imaging necessary for optimal F466N/F470N emission-line selection.

We estimate the local noise in the JELS imaging by placing down 0.3 arcsec diameter apertures in empty regions of the image, with the 1σ noise at a given sky position based on the scatter in the nearest 200 apertures. For a given limiting flux density in f_ν, we then estimate the corresponding maximum emission-line sensitivity, $F_{\rm line}$(erg s^{-1}cm^{-2}), assuming the flux density in the narrow-band is dominated by the emission line (i.e. ~ 0 continuum) or the uncertainty on the continuum estimate from the underlying broad-band (F444W for F466N/F470N, F200W for F212N) is negligible. Note, this conversion also assumes the emission line is centred at the pivot wavelength, $\lambda_{\rm pivot}$, of the narrow-band filter. Finally, the 0.3 arcsec aperture line flux limits are corrected to total fluxes for an assumed point-source based on the corresponding fraction of encircled energy for the respective point-spread function (PSF). The resulting distribution of limiting magnitudes and line fluxes for the F466N imaging is shown by the colour scale in Fig. 3 with the additional depth achieved in the central region of the field clearly visible.

2.3.1 *F466N and F470N narrow-band sensitivity*

To summarize the distribution of limiting line fluxes for the JELS narrow-band mosaics, in Fig. 4 we present the estimated line flux sensitivity as a function of both cumulative area (upper panel) and area per limiting flux ($\log_{10}(F_{\rm line}$/erg s^{-1}cm^{-2}; lower panel). As designed, the F466N and F470N imaging reach broadly comparable depths, but with F470N reaching higher sensitivity over the full field due to the additional group per integration and the additional repeat observations also increasing the maximum sensitivity reached in the deepest part of the field. For both F466N and F470N, the additional depth of the central region is immediately apparent (e.g. the lower panel of Fig. 4).

To summarize the sensitivities reached in the central and overall field areas, Table 1 presents the limiting line flux sensitivities reached for the deepest 35 and 90 per cent of the field (see also the vertical dotted and dashed lines in Fig. 4) in each of the JELS narrow-bands. Also shown in Table 1 is the limiting *observed* Hα luminosity, $L_{\rm H\alpha}$, corresponding to the flux limit for the specified redshifts. The conversion to Hα luminosity includes a correction for the typical expected contribution from [N II]λ6585, assuming $\log_{10}$([N II]λ6585/Hα) $= -1.31$ as measured for high-z galaxies in early *JWST* samples (Shapley et al. 2023, which leads to a 0.021 dex correction to $L_{\rm H\alpha}$). In the remainder of the manuscript, all quoted $L_{\rm H\alpha}$ at $z \sim 6$ are corrected for [N II]λ6585 contribution based on this assumption unless explicitly specified (e.g. $L_{\rm H\alpha+[N\,II]}$).

The measured sensitivity presented in Fig. 4 (and Table 1) compares favourably to the pre-launch predicted sensitivity of 2.2×10^{-18} erg s^{-1}cm^{-2} within a 0.4 arcsec aperture (for an assumed characteristic radius of 0.15 arcsec and Sérsic $n = 1.2$ light-profile) for the areas with $\sim 6\,000$s total exposure, extending down to 1.5×10^{-18} erg s^{-1}cm^{-2} over the central region with double the exposure time. Although formally not the exact same metric, the measured luminosity limits are between ~ 0.2–0.3 dex more sensitive than pre-launch predictions, in line with in-flight performance for NIRCam photometry seen more widely in medium and broad-band imaging (Rigby et al. 2023).

The limiting $L_{\rm H\alpha}$ corresponds to *unobscured* Hα SFRs of 1.9–3.2 M$_\odot$ yr^{-1} based on low-redshift calibrations (Hao et al. 2011), or 0.9–1.3 M$_\odot$ yr^{-1} for SFR calibrations more appropriate for younger stel-

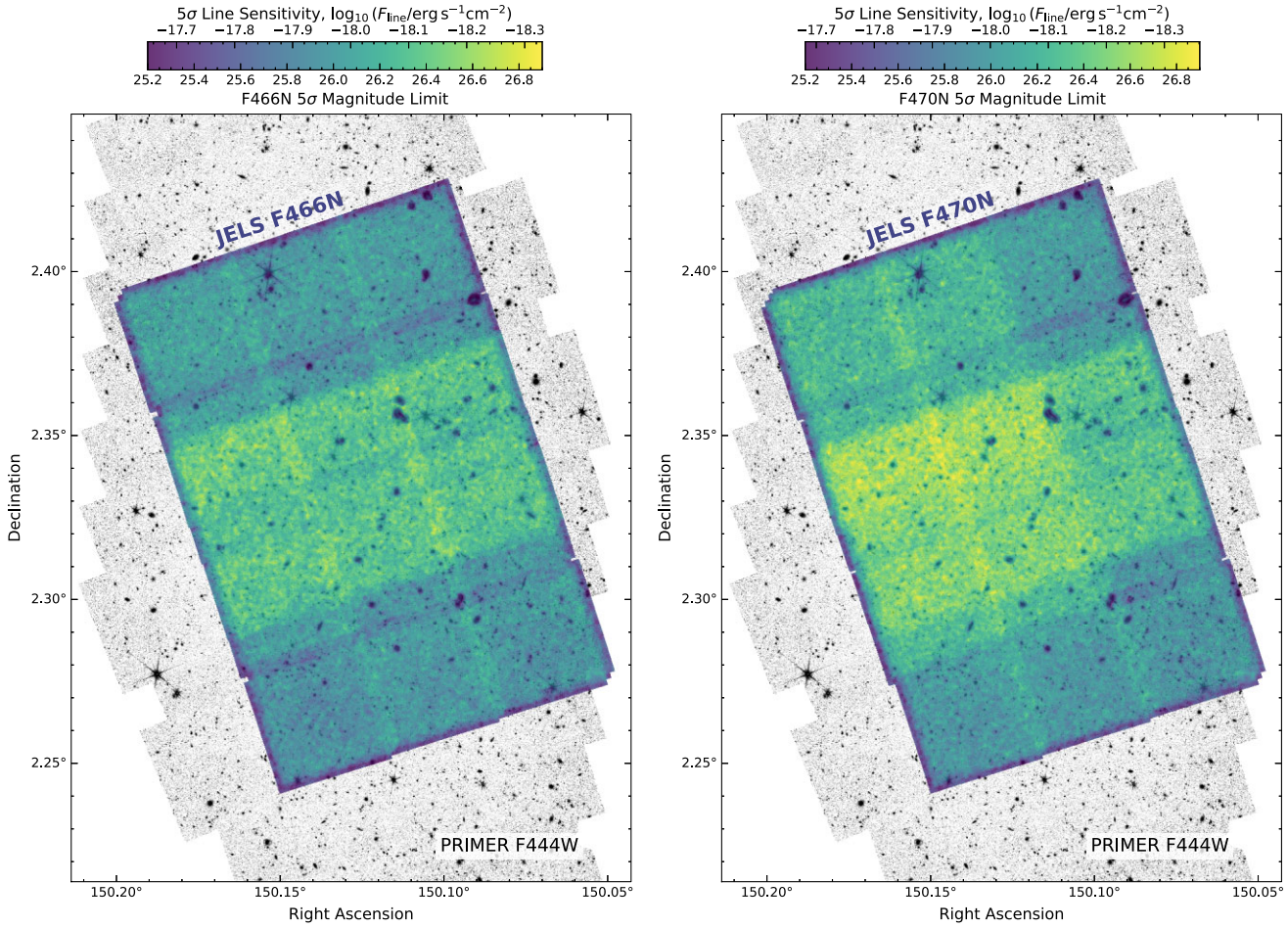

Figure 3. Illustration of the layout and sensitivity of the JELS LW narrow-band imaging within the PRIMER COSMOS field. The background image shows the PRIMER F444W broad-band image with an illustrative image stretch. The 5σ limiting magnitude and corresponding maximum emission-line sensitivity for the JELS F466N (left) and F470N (right) narrow-band imaging are shown by the colour scale, where the local noise at a given pixel is estimated from the nearest 200 0.3 arcsec apertures in empty sky regions. The central $\sim 1/3$rd of the JELS field that has double the exposure time is immediately apparent in both mosaics. Similarly, the overall gain in sensitivity from repeats of observations most severely impacted by scattered light can be seen in the north east quadrant of the F470N depth map.

lar populations at higher redshift ($\log_{10}(L_{\mathrm{H}\alpha}/\mathrm{M}_\odot\,\mathrm{yr}^{-1}) = -41.64$; Theios et al. 2019). We note that the intrinsic Hα luminosity distribution probed, once corrected for dust attenuation, will naturally be brighter. For example, Covelo-Paz et al. (2025) measure an average extinction of $A_{\mathrm{H}\alpha} = 0.47$ for $4 < z < 6.5$ Hα emitters.

Given the $\sim 4.7\,\mu$m sensitivities achieved over the survey area of $\sim 63\,\mathrm{arcmin}^2$, the JELS narrow-band survey probes a complementary parameter space to the 'First Reionization Epoch Spectroscopically Complete Observations' (FRESCO; GO #1895, Oesch et al. 2023) slitless spectroscopy survey, which reaches a 5σ line sensitivity at ~ 4–$5\,\mu$m of 2×10^{-18} erg s^{-1}cm^{-2} (Fig. 4, see also Covelo-Paz et al. 2025). Covering two $\sim 62\,\mathrm{arcmin}^2$ fields (of which 4.4–5 μm is visible over ~ 73 per cent), the wavelength coverage of FRESCO allows un-targeted detection of emission-line sources over a wider redshift range and hence survey volume (plus simultaneous spectroscopic confirmation). While the robust identification of single lines like Hα may be challenging (Baronchelli et al. 2020), continuum-subtracted detection techniques have proven to be highly effective (see e.g. Helton et al. 2024; Meyer et al. 2024, in addition to the citations above) for grism surveys. Although probing a more limited redshift range, the JELS narrow-band is sensitive to fainter line fluxes at $\sim 4.7\mu$m over the full mosaic, reaching up to $\sim 2\times$ fainter in the central region, with no losses due to dispersion off the detector and reduced blending or contamination from bright sources. As such, JELS is able to robustly detect a sample of Hα emitters at $z > 6$ comparable to both FRESCO fields combined, despite the limited volume ($z \sim 6.1$ versus $6 < z < 6.6$, see Section 3.1.1). Additionally, as further discussed in Section 3.2, the narrow-band imaging retains the full two-dimensional (2D) morphological information, providing information on the spatially resolved ionized gas structures of individual galaxies (cf. the ensemble structural information robustly measurable in slitless spectroscopy; Matharu et al. 2024). The two approaches are therefore highly complementary, and combined probe a broader dynamic range of emission-line galaxies in the EoR.

2.3.2 *F212N narrow-band sensitivity*

For the F212N narrow-band, the mosaic reaches a 5σ limiting line flux of 2.5×10^{-18} erg s^{-1}cm^{-2} for the deepest 90 per cent of the field (see Table 1). This depth corresponds to ~ 0.7–0.8 dex fainter Hα luminosities probed at $z \sim 2.2$ than the LW narrow-bands

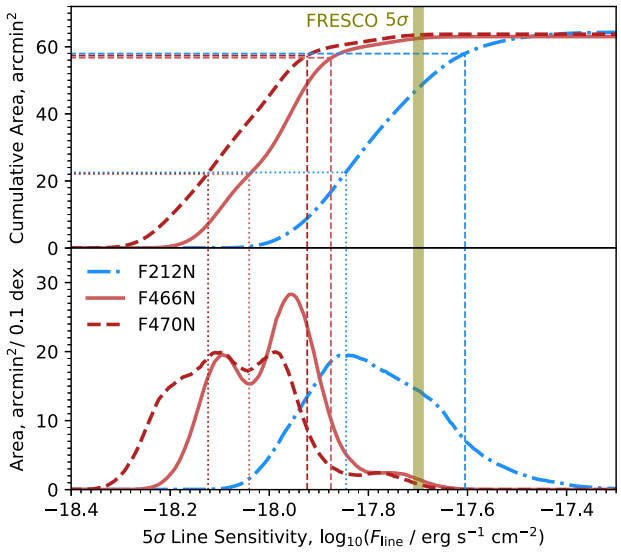

Figure 4. Emission-line sensitivity of the JELS narrow-bands as a function of area covered, both cumulative area (top) and area per limiting sensitivity (bottom). The cumulative area corresponding to the deepest 35 per cent (~ 22 arcmin^2; i.e. the central region with double exposure) and 90 per cent (~ 57 arcmin^2) of the full JELS area are marked with thin horizontal dotted/dashed lines, respectively, with vertical lines where they intersect the sensitivity curve. Exact values are tabulated in Table 1 alongside the corresponding Hα luminosity limit. Also plotted for reference is the average 5σ limiting line sensitivity for Hα sources at $4.9 < z < 6.6$ in the FRESCO slitless spectroscopy survey (thick vertical line; Oesch et al. 2023).

Table 1. Limiting emission-line flux and corresponding observed $L_{\rm H\alpha}$ sensitivity (corrected for [N II]λ6585 contribution) reached for the three JELS narrow-band images shown in Fig. 4, with 5σ point-source limits corresponding to the deepest 35 per cent of the field (~ 22 arcmin^2; i.e. the central region with double exposure) and the deepest 90 per cent (~ 57 arcmin^2). As noted in the main text, intrinsic $L_{\rm H\alpha}$ limits accounting for dust attenuation will be higher than the quoted values.

Filter ($z_{\rm H\alpha}$)	5σ Flux limit $\log_{10}(F_{\rm line}/{\rm erg\ s^{-1}cm^{-2}})$		5σ Luminosity limit $\log_{10}(L_{\rm H\alpha}/{\rm erg\ s^{-1}})$	
	Percentage of the JELS coverage			
	35 per cent	90 per cent	35 per cent	90 per cent
F212N (2.23)	−17.84	−17.60	40.75	40.99
F466N (6.09)	−18.04	−17.88	41.60	41.76
F470N (6.17)	−18.12	−17.92	41.53	41.73

probe at $z \sim 6.1$, reaching $L_{\rm H\alpha} > 10^{40.99}$erg s^{-1} ($10^{40.75}$erg s^{-1} in the doubly imaged area). For the same SFR calibration assumed above (Theios et al. 2019), these limits correspond to unobscured Hα SFRs of 0.13–0.22 M$_\odot$ yr^{-1}. We note that in Fig. 4, the bi-modality corresponding to the central region is less clearly defined for the F212N filter due to the variation in depths from mosaicing of the smaller SW modules and the increased impact of bright stars in the field (cf. the extent of diffraction spikes in Fig. 5 relative to Fig. 3). Nevertheless, the JELS imaging still reaches line sensitivities $\sim 5\times$ more sensitive than the previous state of the art over the full field and almost an order of magnitude more sensitive in the central region (cf. $\sim 10^{41.7}$erg s^{-1}; Geach et al. 2008; Hayes, Schaerer & Östlin 2010; Sobral et al. 2013).

2.3.3 F200W broad-band sensitivity

Finally, in Fig. 5, we illustrate the additional F200W broad-band depth gained in the centre of the PRIMER COSMOS field from the addition of the JELS imaging. The F200W mosaic in COSMOS using only PRIMER imaging reaches an average global 5σ depth of $m_{\rm F200W} = 28.3$ over the best 63 arcmin^2 of the field when the depths are calculated using the same 0.3 arcsec apertures corrected to total flux (we note that the different depths quoted in Donnan et al. 2024 are calculated from PSF homogenized images). With the JELS F200W imaging included, the equivalent deepest area within the field reaches a median depth of $m_{\rm F200W} = 28.7$. We note that in Fig. 5, the impact and extent of bright stars in the field is visibly worse than seen in any of the narrow-band images. We attribute this difference primarily to the significantly increased continuum sensitivity of the F200W image and the resulting increased dynamic range that makes the presence of extended diffraction spikes more visible. The full extent of the brighter stars is already visible in just the PRIMER imaging alone, so other broad-band filters will be affected to a similar degree. Additionally, unlike the diffraction patterns for the narrow-band filters (that are somewhat stippled due to the narrow wavelength coverage), the F200W diffraction spikes are continuous and therefore contribute more to the local noise in these regions. Given the importance of the ancillary data to the narrow-band selection, bright star masks that fully cover the effected regions will need to be incorporated in subsequent scientific analysis (as is standard in the literature).

3 SCIENTIFIC GOALS

3.1 Global line emitter properties

3.1.1 A census of H α emitters at $z \sim 6.1$

The primary goal of the JELS survey is to carry out the first narrow-band Hα survey at $z > 6$, obtaining a sample of $\gtrsim 40$ Hα emitters (Pirie et al. 2025). The JELS Hα sample is designed to provide tight constraints on the faint end of the Hα LF at $z \sim 6$, with sufficient accuracy to constrain the space density of Hα emitters at these luminosities to within 0.1 dex. In addition to providing new integral constraints on the cosmic SFR density of galaxies in the EoR (Madau & Dickinson 2014, see Fig. 1), the JELS $z \sim 6.1$ Hα sample will make it possible to study the nature of star-forming galaxies at this epoch in a relatively unbiased sample and to constrain the scaling relations linking ongoing star formation to key galaxy properties such as masses, sizes (Stephenson et al. in preparation) and clustering properties (Hale et al. in preparation).

Given the high completeness within the survey volume and the range of line fluxes probed, the JELS Hα sample also offers a valuable test-bed for understanding the potential biases and limitations of UV-based selection techniques that are ubiquitously used at high redshifts. For example, the bursty nature of star formation in low-mass galaxies is now understood to play a key role in dictating the observability of high-redshift galaxies (Sun et al. 2023a), and hence significantly impacting on the inferred UV LFs (Sun et al. 2023b), as well as strongly impacting estimates of key galaxy properties such as stellar mass (Endsley et al. 2023) and ionizing photon escape (Flury et al. 2025). With JELS, it is possible to derive the distribution of Hα (~ 10 Myr time-scales) to UV SFRs (~ 100 Myr time-scales) in a homogeneously selected sample of galaxies in the EoR for the first time. By selecting on emission-line strength, the narrow-band selection is naturally sensitive to the highest equivalent

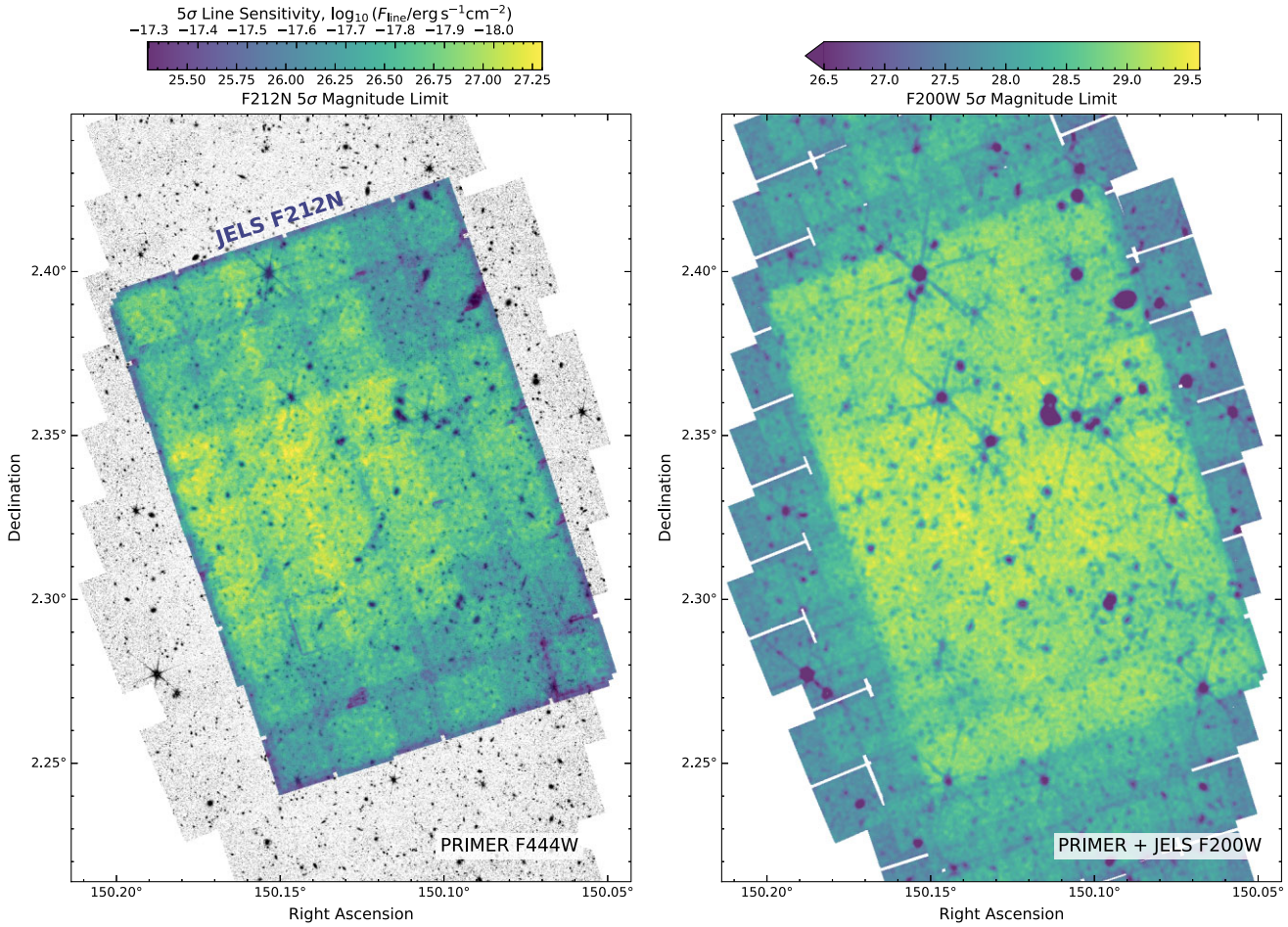

Figure 5. Illustration of sensitivity of the combined PRIMER and JELS F200W imaging in the COSMOS field. The 5σ limiting magnitude and corresponding maximum emission-line sensitivity are shown by the colour scale, where the local noise at a given pixel is estimated from the nearest 200 0.3-arcsec apertures in empty sky regions and corrected to total fluxes given the fraction of encircled energy for the F200W PSF. As for F470N, the overall gain in sensitivity from repeats of observations impacted by scattered light can be seen in the north east quadrant of the F212N depth map.

width population and hence provides constraints on the youngest or most extreme burst populations (see e.g. Maseda et al. 2023). Recent studies with *JWST* medium bands confirm the expectation that high-redshift galaxies displaying evidence for elevated recent star formation activity are typically the most efficient ionizing photon producers (i.e. higher $\xi_{\rm ion}$; Simmonds et al. 2024), while modelling predicts that very high Hα SFRs could correlate with increased ISM porosity (Clarke & Oey 2002) and hence Lyman continuum photon escape. The high EW emission-line sources selected by JELS may therefore offer an especially valuable probe of the most extreme ionizers of the IGM.

Further enhancing the scientific potential of the JELS Hα sample in this area is the ongoing deep Multi Unit Spectroscopic Explorer (MUSE; Bacon et al. 2010) integral field spectroscopy over the full JELS survey footprint (ESO Large Programme 112.25WM.001, PI: Swinbank), reaching triple the exposure time per pointing of the MUSE-Wide Survey (Urrutia et al. 2019) over $\sim 1.75\times$ greater area. The combination of a homogeneously selected Hα sample with complete resolved rest-UV spectroscopy will enable a broad range of studies into the late stages of cosmic reionization, with the potential to improve on and complement existing studies of Lyα emitter fractions (Stark et al. 2010), Lyα emission-line profiles (Mason et al. 2018), constraints on $\xi_{\rm ion}$ as a function of Lyα properties (Prieto-Lyon et al. 2023; Saxena et al. 2024) and resolved studies of Lyα (e.g. Smith et al. 2018; Roy et al. 2023).

Another key advantage offered by narrow-band samples is that they are ideally suited for clustering analyses, as the narrow redshift slice minimizes redshift projection effects (cf. Geach et al. 2012; Cochrane et al. 2017). Measurement of the correlation of Hα emitters at $z \sim 6.1$ will enable constraints on the dark-matter haloes hosting these star-forming galaxies. In addition to placing these sources into their broader cosmological context for direct comparisons with galaxy formation simulations, these measurements will offer another critical comparison against existing Lyman break and Lyα emitter galaxy samples at this epoch (see also Section 3.1.3).

3.1.2 The faint star formation population at cosmic noon

One of the largest uncertainties in constraining the global cosmic SFR density is the precision to which the faint-end slope of respective LFs can be reliably constrained. The faint end of the UV LF has been tightly constrained across the bulk of cosmic history (reaching $M_{\rm UV} > -15$ out to $z > 6$; Bhatawdekar et al. 2019; Bouwens et al. 2022; Harikane et al. 2022), with very tight constraints at cosmic noon (Parsa et al. 2016, $\alpha \pm 0.04$) and clear evidence of steepening slopes as redshift increases. Current constraints on the faint end of

the Hα LF at cosmic noon are, however, significantly more limited (Sobral et al. 2013; Terao et al. 2022). This is a critical measurement, since the difference between a faint-end slope of $\alpha = -1.75$ and $\alpha = -1.5$ corresponds to a factor of 2 difference in the integrated SFR density.

The extreme depth of our *JWST* NIRCam imaging means that the JELS F212N observations will detect Hα emitters $\sim 5\times$ fainter than previous ground-based studies, with an estimated sample size of ~ 200. The resulting determination of the faint-end slope of the $z = 2.23$ Hα LF can achieve a precision of $\delta_\alpha < 0.05$, almost $3\times$ better than current limits, thereby tightly constraining the relative evolution of dwarf galaxies. Furthermore, the extensive broad-band imaging from *HST*/CANDELS and PRIMER will enable robust constraints on the stellar masses, star formation histories and the dust attenuation of the Hα sample.

In addition to the F212N Hα sample constraints at $z = 2.23$, the JELS F466N/F470N filters also probe the Paschen lines Paα and Paβ at $z \sim 1.5$ and 2.6, respectively, bracketing the peak of cosmic star formation (Fig. 1). Essentially unaffected by dust, the Paα (1.87 μm) and Paβ (1.28 μm)-lines offer unbiased instantaneous SFR-indicators (Cleri et al. 2022). For the JELS F466N limiting line flux (90th percentile), the corresponding Paα and Paβ luminosity limits reach $10^{40.25}$ and $10^{40.84}$erg s^{-1}, respectively (0.17 dex deeper in the central region). Assuming Case B recombination, a temperature of 10,000K and electron density, $N_e = 10^4$ cm^{-3}, we expect line intensity ratios of Hα/Pa$\alpha = 8.584$ and Hα/Pa$\beta = 17.614$ (Storey & Hummer 1995). The Paschen line sensitivities at $z \sim 1.5$ (Paα) and 2.6 (Paβ) therefore correspond to equivalent Hα luminosities of $10^{41.18}$ and $10^{42.1}$erg s^{-1}, or SFRs of 0.35 and 3.6M$_\odot$ yr^{-1}, respectively.[3] The Paschen line depths are therefore comparable to, or deeper, than those achieved for existing Hα narrow-band samples at these redshifts (Geach et al. 2008; Sobral et al. 2013). We caveat that recent evidence suggests that the standard Case B assumption may not be valid in all galaxies, both in the lower redshift Universe (Flury et al. 2022; Scarlata et al. 2024) and at the redshifts probed by the JELS Paschen samples (Pirzkal et al. 2024). The inferred limiting SFRs are therefore only illustrative. Statistical samples of bright Paschen line emitters at cosmic noon selected by JELS therefore also offer an ideal test-bed for future spectroscopic studies exploring the diversity of interstellar medium (ISM) conditions in star-forming galaxies through the distribution of Balmer and Paschen line ratios.

3.1.3 The role of galaxies in reionization – [O III] emitters at $8.3 \lesssim z \lesssim 8.5$

Prior to *JWST*, the prevalence of high EW [O III] emitters at $z > 6$ had been studied in large samples based on strong broad-band colour excess (e.g. De Barros et al. 2019), with the [O III] EW found to strongly correlate with redshift (Khostovan et al. 2016). Studies of the properties of [O III] emitters at $z > 6$ from medium/broad-band *JWST* observations (Simmonds et al. 2023; Begley et al. 2024; Wold et al. 2025) and slitless spectroscopy (Matthee et al. 2023) indicate that the highest EW sources are likely to be producing ionizing photons with very high efficiency, and could therefore represent key drivers of the early stages of cosmic reionization. Similar to the Hα selection, homogeneously selected samples of [O III] emission-line sources from JELS can therefore offer a probe of the earlier stages of reionization at $z \sim 8.4$, both through the overall statistical constraints and by sign-posting the sites of the largest ionized bubbles that can then be probed through Lyα transmission modelling (e.g. Tang et al. 2024; Witstok et al. 2024). When the [O III]λ5008 line falls within F466N ($z = 8.298$ at $\lambda_{\rm pivot}$), the narrow-band line flux limits presented in Table 1 correspond to luminosity limits of $L_{\rm [O\,III]\lambda5008} \sim 10^{41.8}$–$10^{41.9}$ erg s^{-1} for the deeper JELS region, increasing to $\sim 10^{42.0}$erg s^{-1} for 90 per cent of the survey area. At slightly higher redshifts, the fainter [O III]λ4960 line is also then redshifted into the narrow-bands (extending up to e.g. $z = 8.492$ at $\lambda_{\rm pivot,F470N}$) with comparable measured line sensitivity. For an assumed intrinsic [O III]λ5008/[O III]λ4960 ratio of 2.98 (Storey & Zeippen 2000), we note however the effective [O III]λ4960 sensitivity is ~ 0.5 dex lower than for [O III]λ5008 selection. The JELS narrow-band imaging is highly complementary to slitless spectroscopic surveys, extending emission-line selections to fainter $L_{\rm [O\,III]\lambda5008}$ at $z > 8$ (cf. Meyer et al. 2024), potentially improving constraints on the faint end of the [O III]λ5008 LF and revealing key populations critical in the process of cosmic reionization. Below we illustrate the exquisite morphological information provided by the narrow-band imaging (Section 3.2) and the reliability and sensitivity of the selection (Section 4).

3.1.4 Other line emitter samples

Finally, while the science cases outlined above focus on intrinsically brighter emission-line species, the combination of high-sensitivity and extensive ancillary observations sufficient to distinguish between potential redshift solutions means that JELS is sensitive to a broad range of novel emission-line sources. Further examples range from the 3.3 μm poly-aromatic hydrocarbon (PAH) feature at $z \sim 0.4$ (F466N/F470N) in the lower redshift Universe, to [S III]λ9069 at $z \sim 4.1$ (F466N/F470N) and [O II]λ3727 at $z \sim 4.7$ (F212N) in the early Universe. Sources with line strengths in intrinsically weaker optical–near-IR line species sufficiently bright to be robustly selected as excess sources in JELS likely represent ideal targets for detailed spectroscopic follow-up. Regardless, the ability to isolate emission lines in narrow-band filters results in improved photometric redshift (photo-z) and SED modelling precision for all such sources, as well as the potential for detailed morphological studies.

3.2 Spatially resolving ionized gas properties

Early *JWST* observations have demonstrated that the preceding picture where regular Hubble-sequence morphologies emerged around cosmic noon ($1 < z < 3$; Mortlock et al. 2013) may not be correct, with discy morphologies potentially dominating the galaxy population as early as $z \sim 7$ (e.g. Ferreira et al. 2022; Kartaltepe et al. 2023; Conselice et al. 2024). Robustly measuring galaxy morphologies at $z > 2$ is crucial for far more than simple galaxy classification. Constraining the spatial distribution of on-going star formation within galaxies as a function of stellar mass (and ideally halo mass), or other key properties such as AGN activity, can directly inform models of feedback in hydrodynamical simulations (Cochrane et al. 2023). One of the key advantages offered by narrow-band emission-line selection over slitless spectroscopic surveys is immediate access to the robust 2D emission-line morphologies in *individual* galaxies. This means that JELS will enable studies of resolved ionized gas properties in less biased galaxy samples on sub-kpc scales without the need for complex forwarding modelling of multiple dispersion directions (Pirzkal et al. 2018; Estrada-Carpenter et al.

[3]Where $\log_{10}(\mathrm{SFR_{H\alpha}}/\mathrm{M_\odot\,yr^{-1}}) = -41.64 + \log_{10}(L_{\rm H\alpha}/\mathrm{erg\,s^{-1}})$ assuming the SFR calibration of Theios et al. (2019).

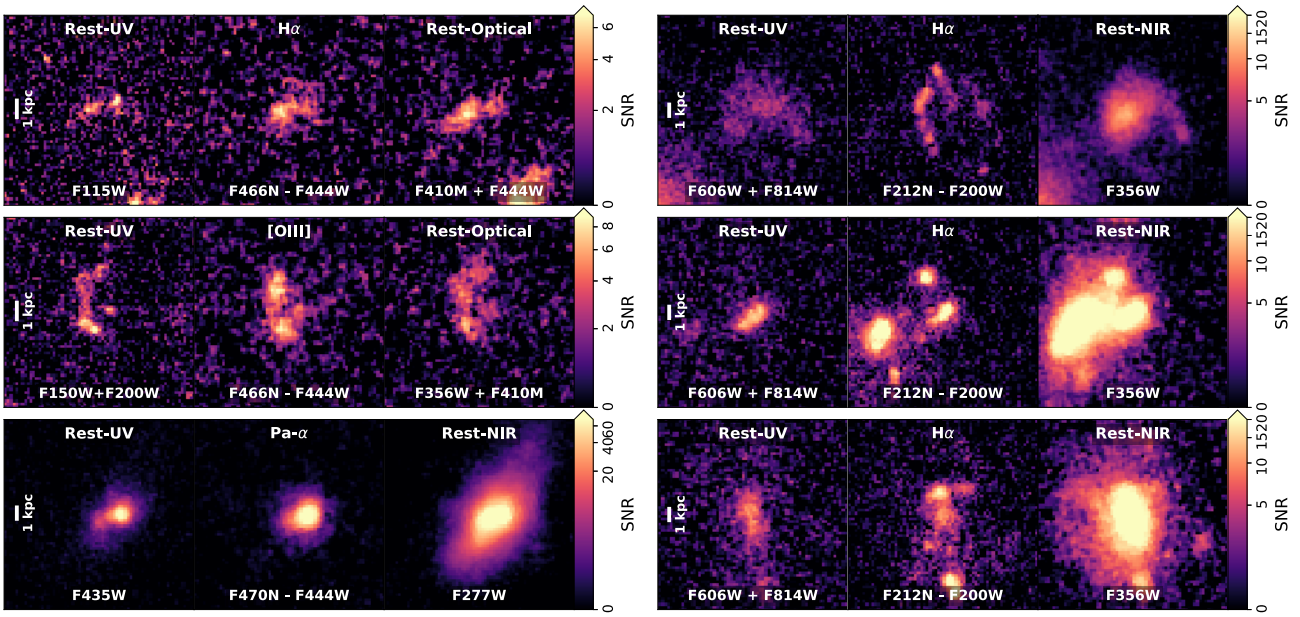

Figure 6. Illustration of resolved rest-UV (left), emission-line (centre) and rest-frame optical/NIR (right) for Hα, [O III] and Paα emission-line objects in JELS. Examples of F466N or F470N-selected sources are shown in the left column, with examples of bright extended F212N excess sources shown in the right column. The corresponding broad and narrow-band filter combinations are indicated in each image. Cut-outs are 2 arcsec $\times$ 2 arcsec in size, with consistent colour scales illustrated by the corresponding colour bar and 1 proper kiloparsec at the corresponding redshift shown for reference.

2024; Shen et al. 2024), or the stacking analysis of statistical samples (Nelson et al. 2013; Liu, Morishita & Kodama 2024; Matharu et al. 2024).

As with integrated measurements above (Sections 3.1.1–3.1.4), this is particularly valuable when the ionized gas offers a direct star formation tracer. The JELS Hα and F466N/F470N Paα/Paβ samples offer a clean probe of sub-L* galaxies at their respective redshifts whose multiwavelength properties, resolved structures, and parametrized morphologies can be compared with those of brighter galaxies (and lower-redshift samples) to investigate the physical processes driving star formation within these galaxies (e.g. Cochrane et al. 2021). In Fig. 6, we show the rest-UV, ionized gas (narrow-band excess) and rest-optical/near-infrared continuum morphologies for examples of both F466N/F470N and F212N excess selected emission-line galaxies. The advantage of resolving both the UV and Hα (or Paα) star formation is immediately evident, with significant variation both between the two star formation probes and the underlying continuum that gives insights into the star formation properties of galaxies that cannot be obtained from one alone (e.g. the distribution of dust, or the variation of star formation timescales within the galaxy). When extended to the full narrow-band samples, JELS can therefore constrain the morphology of on-going star formation compared to that of the *in situ* stellar mass (measured from resolved SED fitting with full PRIMER observations) for a representative sample of SFGs, testing whether the inside-out growth of galaxies inferred from stacks at $z < 1.5$ (Nelson et al. 2016) is true for all individual galaxies and tracing this over a critical period in the morphological history of galaxies.

4 PREDICTED Hα AND [O III]λ5008 REDSHIFT AND EMISSION-LINE RECOVERY

Demonstrating the relevant sensitivity and physical constraints enabled by the JELS narrow-band imaging for all of the potential science cases is impractical given the wide range in emission lines, redshifts and associated physical properties (integrated or resolved) probed. Nevertheless, for the key target samples of Hα and [O III]λ5008 -emitters, it is informative to test the practical ability for JELS to recover emission-line-selected galaxies in narrow redshift slices at $z > 6$, alongside the precision to which corresponding emission-line properties can be estimated. Additionally, we can explore the quantitative advantages offered by narrow-band imaging over existing broad-band imaging alone, or potential alternatives such as medium-band surveys that could probe larger cosmological volumes at the expense of redshift precision.

To generate a range of intrinsic SEDs that span a plausible range in equivalent widths while also providing realistic accompanying continuum and broad-band colours, we use the `Prospector` Bayesian SED modelling code (Johnson et al. 2021b) to efficiently generate stellar population models from the Flexible Stellar Population Synthesis (FSPS; Conroy, Gunn & White 2009; Conroy & Gunn 2010; Johnson et al. 2021a) package, with accompanying CLOUDY (Ferland et al. 2013) photo-ionization nebular line and continuum emission as outlined in Byler et al. (2017).

To avoid unnecessary duplication and analysis, we make the simplifying assumption that any conclusions drawn from an F466N sample will be largely applicable to an F470N-selected sample, or that the increased sensitivity of F470N would only result in increased precision or sensitivity. For each of the emission-line samples, we therefore generate a full parent sample of mock galaxies over a range of redshifts corresponding to just the JELS F466N wavelength coverage. At each redshift step, we generate 1000 mock galaxy SEDs with a range of stellar population parameters designed to ensure that the emission-line equivalent widths extend below the range expected for real galaxies samples at these redshifts (e.g. Endsley et al. 2024). The redshift ranges and corresponding ages for each sample are chosen to be as follows:

(i) Hα : Redshifts spanning $6.06 < z < 6.12$ with a step size of $\delta z = 0.01$. For all redshift steps, the time since the onset of star formation, t_{age}, for a constant star formation history (CSFH) is drawn from a log-uniform prior in the range $-2.3 < \log_{10}(t/\mathrm{Gyr}) < -0.15$.
(ii) [O III]λ5008 : Redshifts in the range of $8.25 < z < 8.35$ with $\delta z = 0.01$, and a corresponding CSFH t_{age} distribution from $-2.3 < \log_{10}(t/\mathrm{Gyr}) < -0.37$.

For both mock galaxy samples, metallicity is drawn from a flat distribution in $\log_{10}(Z/Z_\odot)$ in the range of $-0.7 < \log_{10}(Z/Z_\odot) < -0$ (with the assumption that $Z_{gas} = Z_{stellar}$). Additionally, to allow for a plausible variation in emission-line properties the ionisation parameter, $\log_{10}(U)$, is drawn from a range appropriate for the metallicity ($-3 < \log_{10}(Z/Z_\odot) < -2$, see e.g. Reddy et al. 2023). For dust attenuation, we assume a simple Calzetti et al. (2000) dust attenuation law with extinction magnitude, A_V, drawn from a log-normal distribution with a mean of $\ln(A_V) = -1.69$ (i.e. $A_V = 0.18$) and standard deviation of 0.5. The specific distribution values are chosen to broadly to match the typical attenuation estimated for the real observed Hα emitter sample (Pirie et al. 2025).

For the simulated SED population, we generate the corresponding intrinsic flux densities in the *Hubble Space Telescope* (*HST*) Optical (ACS/WFC F435W, F606W, and F814W), PRIMER NIRCam and JELS F466N/F470N filters (see table 1 of Pirie et al. 2025). Additionally, to enable simulation of an equivalent medium-band emission-line selection survey, we also generate photometry in the NIRCam/F460M ($\lambda_{pivot} = 4.63\,\mu\mathrm{m}$, $W_{eff} = 0.23\mu\mathrm{m}$) that encompasses the JELS LW narrow-band filters. The 'true' Hα /[O III]λ5008 emission-line luminosities and equivalent widths are measured directly from the corresponding noise-free model spectra. We note that the Hα measurements do not account for underlying Balmer absorption, however for the purposes of this experiment we determine that any resulting systematics are negligible on the basis that the young stellar populations and corresponding high equivalent widths probed by these high-redshift sources means such corrections will typically be minimal. With the emission-line properties measured, the parent SED sample and the corresponding mock photometry is renormalized to a constant line luminosity of $L_{line} = 10^{41}\mathrm{erg\ s^{-1}}$.

For the subsequent analysis, the mock galaxy samples and associated photometry are then scaled to create 10 different samples with intrinsic emission-line luminosity (Hα , [O III]λ5008) spanning the ranges of $41 \leq \log_{10}(L_{H\alpha}/\mathrm{erg\ s^{-1}}) \leq 43$ and $41.3 \leq \log_{10}(L_{[\mathrm{O\ III}]\lambda5008}/\mathrm{erg\ s^{-1}}) \leq 43.3$, respectively. Photometric uncertainties for each filter are drawn from a Gaussian distribution with a standard deviation set by the median uncertainties measured for faint sources in 0.3″diameter apertures in the PSF-homogenized images and associated catalogues presented by Pirie et al. (2025). For simplicity, we assume that the mock galaxies are point sources and for the target PSF in the JELS PSF-homogenized photometry catalogues, the 0.3″aperture captures 50.3 per cent of the total flux of a point source. We therefore correct the simulated SNR accordingly.

For the simulated F460M filter, for which current imaging does not exist, we assume a typical depth that is twice as sensitive as measured in the existing PRIMER F410M imaging. Given that the instrumental sensitivity for F410M is approximately twice that of F460M for the same equivalent exposure time,[4] the F460M sensitivity for our mock medium-band survey therefore corresponds to $\sim 16\times$ the PRIMER F410M exposure time and equivalent to observing for the combined F466N and F470N exposure times.

[4]See e.g. https://jwst-docs.stsci.edu/jwst-near-infrared-camera/nircam-performance/nircam-sensitivity

4.1 Photometric redshift precision of narrow-band selected samples

To explore the practical photo-z precision achieved for a JELS narrow-band selection, we first run the mock emission-line galaxy sample through photo-z analysis comparable to that applied to either real JELS samples or other *JWST*-selected broad-band samples. To enable like-for-like comparison, we perform photo-z analysis for the mock sample using three different subsets of *JWST* NIRCam filters: the full PRIMER filter-set plus JELS LW narrow-band filters (F466N/F470N), the PRIMER filters supplemented with the deep F460M medium-band filter, and a PRIMER-only run. The same *HST* optical filters (F435W, F606W, and F814W) are included for all three runs.

We measure photo-zs using the EAZY (Brammer, van Dokkum & Coppi 2008) template fitting code using the default `fsps` set supplemented with the high-z appropriate templates of Larson et al. (2023b). Since the photometry is completely synthetic, we do not perform any photometric zero-point offset corrections as part of the photo-z analysis. However, we do include an additional 5 per cent systematic uncertainty (added in quadrature) during the template-fitting analysis. We quantify the precision of the resulting photo-z estimates as a function of intrinsic line luminosity and rest-frame equivalent width using two metrics. Firstly, we define the metric, Δ_z, as the redshift range that spans between the 16th and 84th percentiles of the stacked photo-z posterior of all galaxies in a given bin, i.e. $z_{84} - z_{16}$ where for example z_{84} is defined such that $\int_0^{z_{84}} \mathrm{CDF}(z)\,\mathrm{d}z = 0.841$. Secondly, we calculate the robust scatter of a given bin, σ_{NMAD}, defined as as follows:

$$\sigma_{\mathrm{NMAD}} = 1.48 \times \mathrm{median}(|\delta z|\,/(1 + z_{\mathrm{true}})), \quad (1)$$

where $\delta z = z_{\mathrm{phot}} - z_{\mathrm{true}}$. Together, these metrics give a picture of both the typical precision to which an individual galaxy's redshift can be constrained (Δ_z) and the overall sample precision (σ_{NMAD}). Note that the *catastrophic* outlier fraction (i.e. $\delta z/(1 + z_{\mathrm{true}}) > 0.15$) was also investigated as a metric. However, for the majority of the emission-line parameter space probed, in the narrow-band and medium-band photo-z runs the outlier fractions were exactly zero such that any quantitative comparison was uninformative.

In Fig. 7, we present the resulting photo-z statistics for both the simulated Hα and [O III]λ5008 emission-line samples. To determine whether a given source would be included in the corresponding photometric sample, we apply an SNR cut similar to that applied in real sample selections (Pirie et al. 2025). For all three filter sets, we require $f_{\mathrm{F444W}}/\sigma_{\mathrm{F444W}} > 5$ as well as $f_{\mathrm{F356W}}/\sigma_{\mathrm{F356W}} > 3$. Additionally, for the narrow-band and medium-band runs we require $f_{\mathrm{F466N}}/\sigma_{\mathrm{F466N}} > 5$ and $f_{\mathrm{F460M}}/\sigma_{\mathrm{F460M}} > 5$, respectively.

We observe a number of trends in photo-z precision as a function of intrinsic properties that are consistent across both emission-line samples. Firstly, there is a consistent correlation between increased emission-line luminosity and improved photo-z precision in both metrics (i.e. lower σ_{NMAD} and Δ_z). This correlation is to be expected as the line-luminosity most directly correlates with photometric signal-to-noise ratio. Secondly, both the individual and ensemble photo-z precision achieved when JELS narrow-band filters are included is typically ≈ 2–$5\times$ better than the mock medium-band survey for the equivalent intrinsic properties (cf. the effective width of the F460M filter being $\approx 4\times$ wider than the F466N filter). The improvement in Δ_z gained from the medium-band filter when

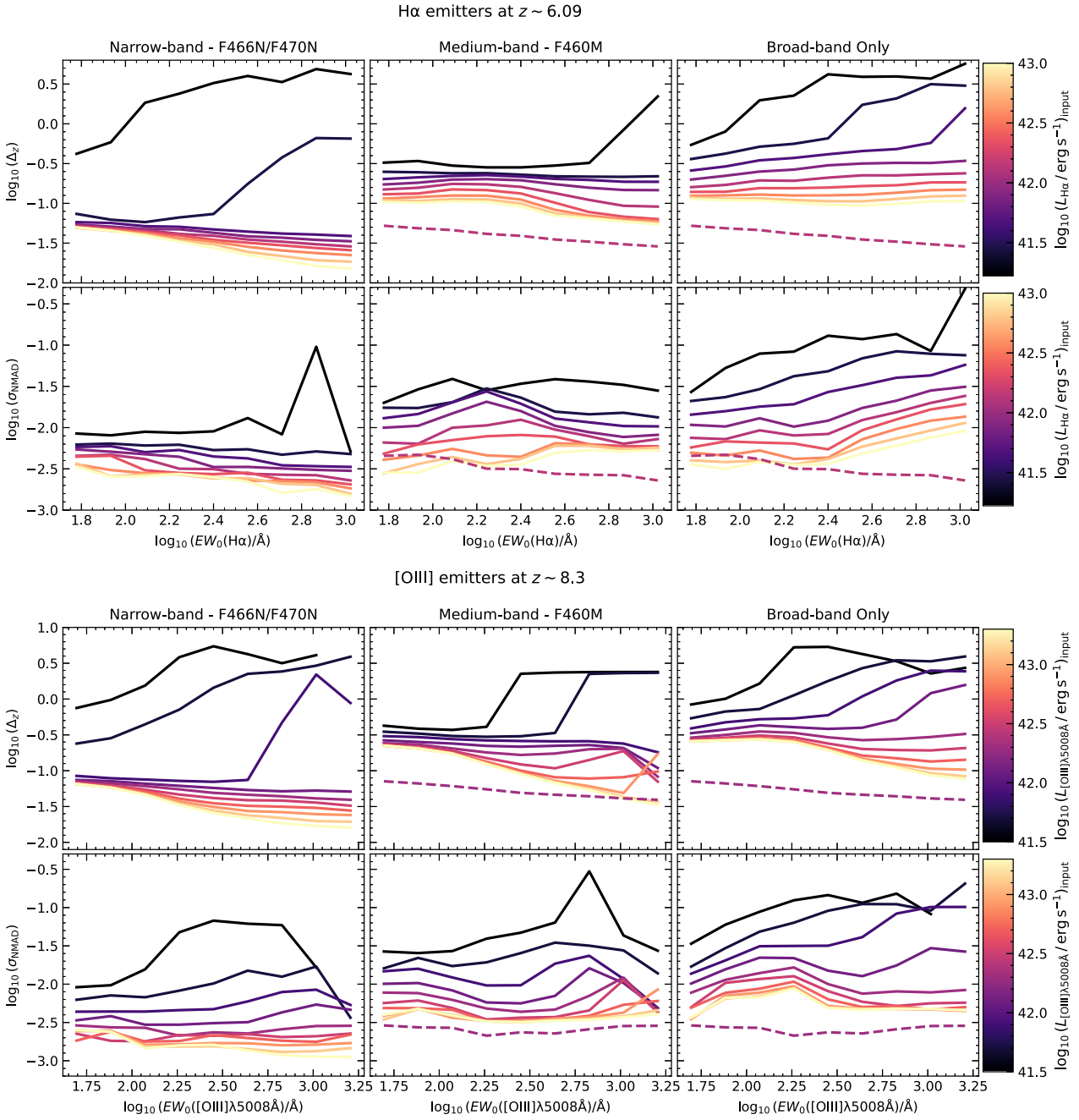

Figure 7. Photo-z statistics, Δ_z and $\sigma_{\rm NMAD}$, as a function of rest-frame equivalent width EW_0 (x-axes) and intrinsic line-luminosity (colour-scale) for the simulated Hα (top) and [O III]λ5008 (bottom) emission-line galaxy samples. For each sample, we present the statistics when both JELS LW narrow-bands are included, when extremely deep F460M medium-band filter is included, and when using the PRIMER filters only (left, centre, and right columns, respectively). To aid comparison, on the middle and right-hand columns the dashed line illustrates the corresponding narrow-band sample statistics for an intrinsic line luminosity close to $L^\star$ (specifically the bins centred at $\log_{10}(L_{\mathrm{H}\alpha}/\mathrm{erg\ s^{-1}}) \sim 42$ and $\log_{10}(L_{[\mathrm{O\,III}]\lambda5008}/\mathrm{erg\ s^{-1}}) \sim 42.3$).

compared to PRIMER-only is less significant, while for a large fraction of parameter space the medium-band survey yields no significant improvement in $\sigma_{\rm NMAD}$ for the same comparison.

We do, however, see variations in the relative improvement when including a narrow-/medium-band, as a function of EW_0. For low rest-frame equivalent widths ($\mathrm{EW}_0 < 200$Å), the dependence of Δ_z on line luminosity becomes negligible. By construction, since the input SEDs are normalized to a given line-luminosity, lower equivalent width sources will have correspondingly brighter stellar continuum and hence higher SNR in their broad-band photometry. The convergence in photo-z statistics at lower-EW_0 when narrow-band filters are included illustrates the parameter space where the photo-z precision is no longer dictated by the precision to which the relevant emission line can be constrained, but instead dominated by other broad-band features such as the Lyman and Balmer breaks. In this regime, there is still, however, a significant improvement from the inclusion of narrow-band, while corresponding medium-band estimates offer only marginal gains over broad-band only

estimates. The majority of $z > 6$ galaxies are expected to have significantly stronger emission-line contributions; Endsley et al. (2024) estimate the typical $EW_0(H\alpha)$ for $z \sim 6$ galaxies ranges from ~ 580 to 850Å ($\log_{10}(EW_0(H\alpha)/Å) \sim 2.8$). Fig. 7 therefore demonstrates that for the expected emission-line luminosities probed by JELS Hα and [O III]λ5008 samples (see Table 1), the inclusion of narrow-band filters should yield samples with typical photo-z scatter $\sigma_{NMAD} \lesssim 0.005 \times (1+z)$ and with individual photo-zs constrained to $\Delta_z \lesssim 0.03$. Furthermore, we note that for input line luminosities of $L_{OIII,input} > 10^{42}$ erg s^{-1}, the JELS narrow-bands are able to constrain the redshift in individual sources to $\Delta_z < 0.08$. Compared to the redshifts of [O III]λ4960 and [O III]λ5008 at the pivot wavelength of the F466N narrow-band filter ($z = 8.29$ and $z = 8.38$, respectively), this illustrates that the combination of both JELS narrow-bands and PRIMER photometry enables sufficient photo-z precision to reliably identify and isolate individual [O III] lines. In contrast, the medium-band photo-z estimates are only able to achieve such precision for the most luminous and highest-EW [O III]λ5008 emitters.

The increased precision from NB-based photo-zs is particularly advantageous for enabling efficient follow-up observations with ALMA to study far-infrared molecular lines (e.g. Carniani et al. 2017; Le Fèvre et al. 2020; Bouwens et al. 2022). The predicted photometric precision corresponds to $\pm$ 600–1700 km s^{-1}, sufficient to ensure the redshifted [CII] 158 µm or [OIII] 88 µm lines would fall into a 3.75-GHz ALMA side band in band 6 or 7, respectively. In Section 5, we further illustrate the practical photo-z precision achieved with real JELS-selected emission-line galaxies for which spectroscopic redshifts have been obtained.

4.2 Sensitivity and accuracy of emission-line recovery

Building on the results above, it is also instructive to explore the corresponding accuracy of the emission-line luminosity that can be recovered from the JELS narrow-band excess emission. For a simulated galaxy to be 'selected' as an emission-line excess source, we require the same individual filter SNR cuts as outlined above in Section 4.1, an emission-line excess significance of $\Sigma > 3$ (equation 2 of Pirie et al. 2025) and that over 50 per cent of the photo-z posterior lies within the range $6.06 < z < 6.12$ for Hα emitters or $8.25 < z < 8.35$ for [O III]λ5008 emitters. For Hα emission-line fluxes from the simulated photometry, we follow the standard prescription for estimating the line-flux based on the observed narrow-band excess (Sobral et al. 2013; Pirie et al. 2025):

$$F_{H\alpha} = \Delta\lambda_{F466N} \frac{f_{\lambda,F466N}\ f_{\lambda,F444W}}{1\ (\Delta\lambda_{F466N}/\Delta\lambda_{F444W})}\ \mathrm{erg\ s^{-1}cm^{-2}}, \quad (2)$$

where $f_{\lambda,i}$ is the measured flux density in filter i, in units of erg s^{-1}cm^{-2}Å^{-1} and the corresponding filter effective widths, $\Delta\lambda_i$ in Å. We also subtract a constant 0.021 dex correction to account for the contribution of [N II]λ6585 to the narrow-band emission, both for consistency within this manuscript (cf. Section 2.3.1) but also to illustrate the validity of this approach in a more realistic application. For [O III]λ5008 , a similar approach can be taken. However, due to the very narrow rest-frame wavelength probed by the JELS narrow-bands at $z \sim 8.3$, accurately estimating the [O III]λ5008 luminosity requires correcting for an additional contribution from [O III]λ4960 that contributes to the narrow-band flux only at some redshifts. While small, these corrections are non-negligible given the high emission-line equivalent widths of galaxies at this redshift. In Appendix B, we outline how we account for these corrections and the changes required to equation (2) for measuring [O III]λ5008 line luminosities.

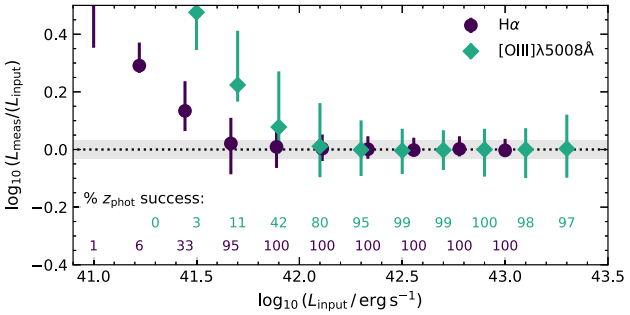

Figure 8. Measured emission-line luminosities, L_{meas}, as inferred from the F466N narrow-band excess relative to the true intrinsic line luminosities, L_{input}, for the simulated Hα (purple circles) and [O III]λ5008 (teal diamonds) samples. For each bin in input luminosity, we show the median and 16–84th percentiles of measured to input line luminosity for a random sub-sample weighted to produce the expected EW distribution (see the text). The shaded horizontal region illustrates 0 ± 0.02 dex. Also shown are the fraction of simulated galaxies in each weighted sub-sample that pass the photo-z selection criteria. Altogether, this figure illustrates that for emission lines above the 5σ limits (see Table 1), JELS can reliably select > 95 per cent of line-emitters and accurately measure the apparent line luminosity with negligible bias and with typical precision of 5 (Hα) to 10 per cent ([O III]λ5008).

As with the photo-z simulation above, our mock emission-line galaxy sample allows us to calculate the accuracy of narrow-band estimated emission-line luminosities as a function of both true input luminosity and rest-frame equivalent width. For the purpose of visualization, and to provide an illustration of the realistic average accuracy, we instead choose to estimate the average accuracy marginalized over the expected EW_0 distributions for Hα at $z \sim 6$ and [O III]λ5008 at $z \sim 8$. We base our assumed EW_0 distributions on the observational results from *JWST* photometric samples, specifically using the inferred Hα EW_0 distribution for 'faint' galaxies from Endsley et al. (2024) with a lognormal distribution of mean $\mu_{EW_0} = 580$ Å and width $\sigma_{EW_0} = 0.26$ dex. For [O III]λ5008 , we assume a lognormal distribution with $\mu_{EW_0} = 380$ Å and $\sigma_{EW_0} = 0.4$ dex, broadly consistent with the [O III] + Hβ EW_0 distributions inferred by Endsley et al. (2024) and Begley et al. (2024) with the mean scaled based on the assumed ratio of [O III]λ5008 /[O III]λ4960 = 2.98. For each input luminosity bin we make 100 draws from the photo-z posterior of each source (see Appendix B) in the bin before randomly selecting 500 samples with a probability weighting based on the assumed EW_0 distribution.

In Fig. 8, we present the resulting distribution of measured to 'true' line luminosity measured directly from the original noise-free simulated spectrum. For each luminosity bin, we show the median measured to input luminosity ratio, with error bars indicating the 16–84th percentiles of the distribution. We see that for both emission-line samples, at bright intrinsic luminosities the narrow-band estimated luminosities are measured to both a high accuracy (with bias < 0.01 dex) and to good precision, with a scatter of ~ 0.02–0.05 dex for Hα and $\sim 0.05 - 0.1$ dex for [O III]λ5008 . For input luminosities close to and below the expected 5σ detection limit (see e.g. Table 1), the average measured luminosity becomes significantly biased relative to the input population. The bias arises from the fact that the intrinsic fluxes for the faint sources are near or below the flux limits for the narrow-band filter, so the subset of sources that pass the selection criteria are those that are scattered above the detection threshold and hence the resulting average inferred luminosity is biased high. To support this conclusion, in Fig. 8 we also show the percentage of the simulated sample (again weighted by

EW_0) in each luminosity bin that passes the individual SNR, excess and photo-z selection criteria. For the luminosity bins exhibiting significant bias ($L_{H\alpha,input} < 10^{41.5}$ erg s^{-1}, $L_{OIII,input} < 10^{42}$ erg s^{-1}), the fraction of galaxies passing the selection criteria is below 50 per cent.

4.3 Summary of simulation results

Together, the simulation results for photo-z precision and line recovery presented here illustrate that for any emission-line sample with luminosities above the 5σ detection limit, the photo-zs should be constrained to extremely high precision ($\sigma_{NMAD} < 0.005 \times (1+z)$). The inferred narrow-band luminosities measured from JELS will also be both accurate ($\pm$0.02–0.1 dex) and precise ($\pm$0.01 dex), with the uncertainties for scientific analysis therefore likely dominated by factors such as the dust attenuation corrections required to estimate intrinsic emission-line luminosities – a limitation true also true for slitless spectroscopic samples and many spectroscopic surveys.

We caveat however that these simplified simulations do not account for realistic extended morphologies, which will decrease the precision of any estimates through both increased noise and systematic uncertainties from measuring *total* fluxes. Future JELS studies will incorporate more extended completeness simulations that account for the full range of observed morphologies and sizes (Pirie et al. in preparation). Furthermore, we have presented simulation results only for sources where the line species of interest falls within the target JELS narrow-band. Therefore, while we have demonstrated that the JELS narrow-band filters provide substantial gains in photo-z accuracy within the target redshifts, *JWST* medium-band surveys will naturally offer the advantage of probing the high-EW_0 lines over a wider redshift range (e.g. Suess et al. 2024, see also Muzzin et al. 2025) and provide complementary constraints to JELS.

5 SPECTROSCOPICALLY CONFIRMED JELS EMITTERS

To further illustrate the diversity of galaxy properties present within the populations selected by JELS and the efficacy of the narrow-band selection, here we present spectroscopic confirmations of four high-z line emitters selected by JELS that were included as filler targets in the Director's Discretionary program DD 6585 (PI: Coulter).

The JELS sample configured in the NIRSpec PRISM observations was selected from a F466N detected catalogue with $SNR_{F466N} > 5$ in 0.3 arcsec apertures. All sources satisfy emission-line excess criteria with colours F444W $-$ F466N > 0.3 and F470N $-$ F466N > 0.15 (corresponding to a rest-frame equivalent width of $EW_0 \gtrsim 20$Å) and with emission-line excess significance, $\Sigma > 3$ (see equation 2 of Pirie et al. 2025). Photo-zs derived from PSF homogenized photometry from all available *HST*/ACS, *HST*/WFC3, and *JWST*/NIRCam filters identified all sources as secure high-z ($z > 5.5$) candidates.[5] The resulting photo-z posteriors are shown in Fig. 9 (solid lines), along with the corresponding photo-z posteriors for the same sources when only the PRIMER NIRCam photometry is used (dashed lines). Of

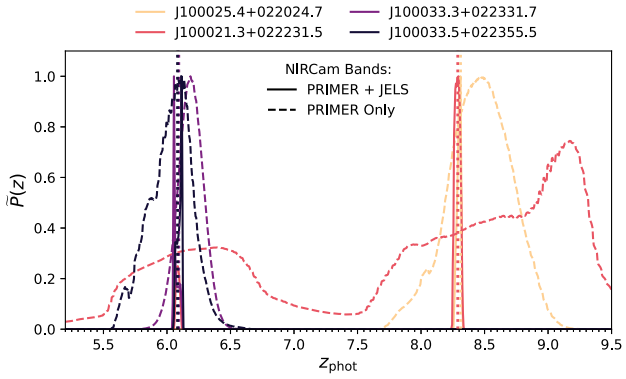

Figure 9. Normalized photo-z posteriors, $\widetilde{P}(z)$, with (solid lines) and without (dashed lines) the inclusion of the JELS F466N and F470N filters for the spectroscopically confirmed line emitters. Due to the extremely narrow posteriors when JELS narrow-band filters are included, the photo-z posteriors have been normalized by their maximum a posteriori values to aid visual comparison. Spectroscopic redshifts from the DDT Prism observations are illustrated by corresponding vertical dotted lines.

the four JELS emission-line candidates observed with NIRSpec, two are robustly identified as Hα emitters with well constrained photo-zs at $z \sim 6.1$, with the other two robustly identified as $z \sim 8.3$ [O III]λ5008 emitters.

In Fig. 10, we show a subset of the available *HST* and *JWST*/NIRCam cut-outs for each object as well as the standard MAST pipeline reduced 2D and 1D PRISM spectra. Motivated by the expectation of high-EW emission-lines, we derive spectroscopic redshifts from the 1D PRISM spectra through a simple χ^2-minimization, fitting an emission-line template (convolved to the PRISM spectral resolution at 4.6 µm) to the continuum-subtracted spectrum over the wavelength range of $3 < \lambda < 5$ µm.[6]

The two confirmed Hα sources are shown in the top row of Fig. 10, observed with exposure times of 5 909 and 17 725s respectively. JELS J100033.5 + 022355.5 (upper left panel) is representative of a large fraction of the Hα emitters selected by JELS, with the overall spectral energy distribution (SED) dominated by high equivalent width (EW) emission lines. The high-EW emission-line contribution can be inferred from the photometry cut-outs alone, with [O III] and Hβ responsible for the F356W broad-band showing clearly elevated flux; this is confirmed by the PRISM spectroscopy. In comparison, JELS J100033.3 + 022331.7 (upper right panel) exhibits significant UV and optical continuum detections across the broad-band SED, although F356W is still significantly enhanced relative to F277W. The corresponding PRISM spectrum reveals significantly lower EW emission-lines, with evidence for a more evolved stellar population in the form of a clear Balmer break. While both sources are correctly identified as $z \sim 6$ sources when using only PRIMER observations, with the spectroscopic redshift contained within the photo-z posterior, the widths of the photo-z posteriors are significantly broader than the PRIMER + JELS estimates by up to $\sim 10\times$ (consistent with the results from Section 4.1).

The bottom row of Fig. 10 then presents the two [O III]λ5008 -emitters selected from JELS, both with total on-source exposure times of 11 817s. The left-hand source, J100021.3 + 022231.5, is

[5]The photo-zs were estimated using EAZY (Brammer et al. 2008) with three different template sets: the default `fsps` set supplemented with the high-z templates of Larson et al. (2023b), the SFHZ set supplemented with the obscured AGN template of Killi et al. (2024) and the EAZY_v1.3 set. The consensus photo-zs combining all three estimates are derived following the procedure outlined in Duncan et al. (2019). See Pirie et al. (2025) for full details.

[6]Our derived spectroscopic redshifts are all in agreement with the independently derived estimates from the DAWN *JWST* Archive: https://s3.amazonaws.com/msaexp-nirspec/extractions/nirspec_graded_v3.html.

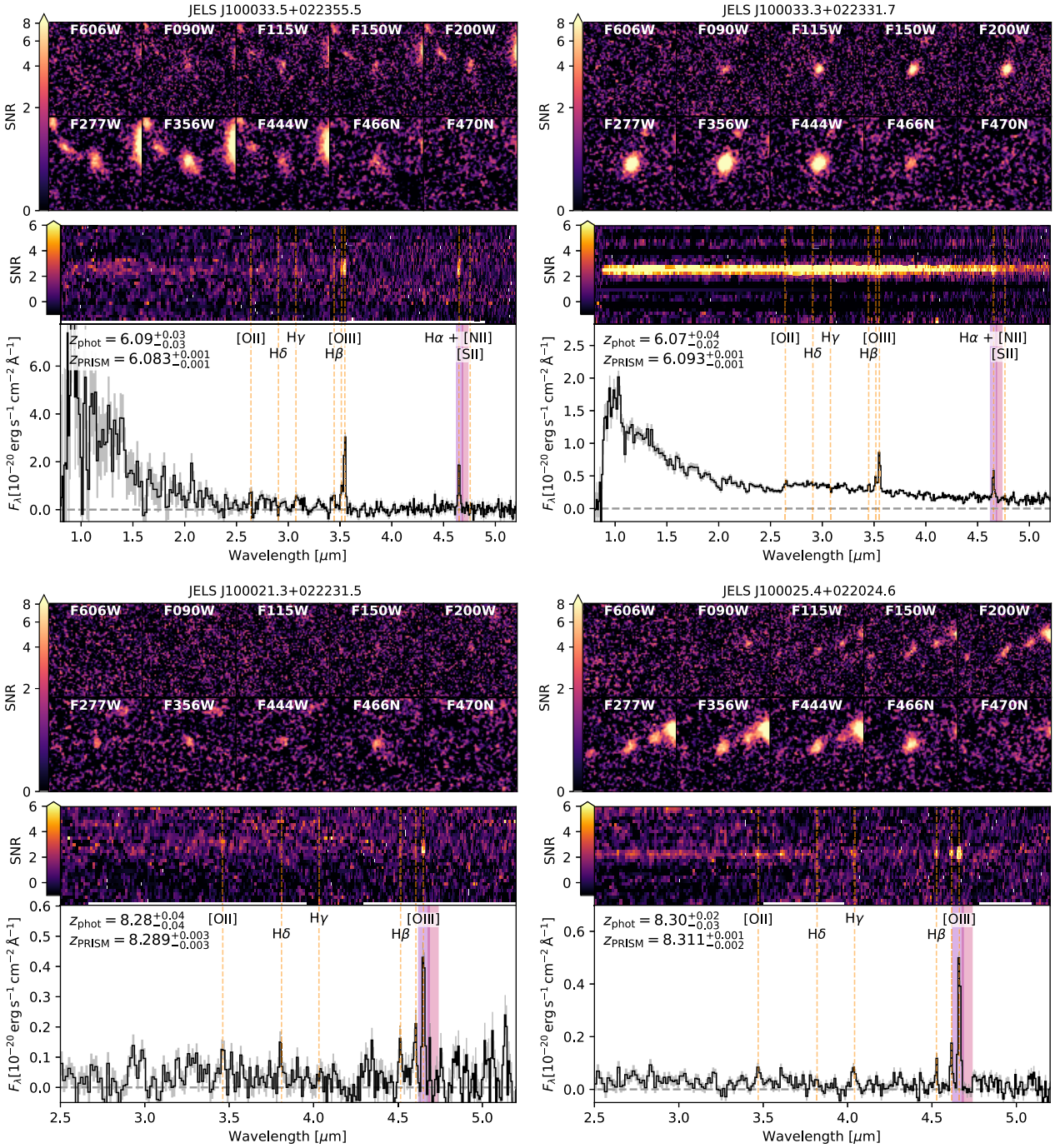

Figure 10. Example emission-line sources selected in JELS narrow-band imaging with spectroscopic confirmation from NIRSpec PRISM spectroscopy (DD 6585, PI Coulter). For each source, the upper panel shows photometry cut-outs (2 arcsec × 2 arcsec) from HST/ACS (F606W) and JWST/NIRCam from both PRIMER and JELS. The lower panel for each source shows the corresponding standard pipeline reduced 2D and 1D PRISM spectra. A subset of bright rest-frame optical emission lines at the confirmed spectroscopic redshift are illustrated by the vertical dashed lines and corresponding labels. Shaded regions also show the wavelength coverage of the overlapping F466N and F470N filters for reference. The top row shows sources selected as H α emitters, while the bottom row shows sources selected as robust $z \sim 8.3$ [O III]λ5008 emitters. Note that at $z \sim 8.3$, the width of the F466N/F470N narrow-bands is such that [O III]λ4960 and [O III]λ5008 (and potentially H β) can be individually isolated from photometry alone.

securely identified as a $z \sim 8.3$ [O III]λ5008 emitter by the photo-z analysis to a precision of $< 0.005 \times (1+z)$, despite having only weak constraints on the Lyman break and very faint rest-UV continuum. With $\mathrm{SNR_{F115W}} < 1$ and $\mathrm{SNR_{F150W}} < 4$ (in 0.3-arcsec diameter apertures), photo-z estimates using broad-band photometry only are limited to constraining the source as $z \gtrsim 5$, but with a very broad posterior allowing solutions up to $z > 10$ (see Fig. 9). Although faint, the extracted 1D PRISM spectrum for this source shows clear H β, [O III]λ4960, [O III]λ5008 and [O II]λ3727 lines confirming the photo-z redshift solution. The right-hand source,

J100025.4 + 022024.6, is selected as a narrow-band excess by JELS, but is also bright enough in the rest-UV to be robustly selected as $z \sim 8$ from broad-band photometry with over 90 per cent of the PRIMER-only photo-z posterior in the range of $8 < z < 9$ (and hence was also included in the DD filler programme from an independent selection). We note that the rest-UV continuum is detected in the NIRSpec PRISM observation, however, we limit the wavelength range of the PRISM spectra presented in Fig. 10 to $> 2.5\mu$m to demonstrate the resolved [O III]λ4960 and [O III]λ5008 lines.

Although only a limited sample, the confirmation of all four narrow-band excess selected sources and their diverse properties gives evidence that JELS offers a broad and robust selection in novel parameter space. In addition to enabling unique science from the photometric data alone, the JELS emission-line samples are therefore ideal for future spectroscopic studies.

6 SUMMARY

We have presented an overview of JELS, a *JWST* imaging survey designed to extend selection of emission-line galaxies using narrow-band filters into new redshift regimes using the *JWST*/NIRCam F466N and F470N filters. Simultaneously, JELS aims to provide a window into the resolved properties of star-forming galaxies at cosmic noon with matching F212N and F200W observations. The JELS Cycle 1 observations presented cover ~ 63 arcmin^2 within the wider PRIMER COSMOS legacy field (Dunlop et al. in preparation), which provides both the key F444W broad-band imaging necessary for F466N/F470N excess selection as well as extensive multiwavelength imaging required for robust line identification.

We have demonstrated that the JELS imaging reaches the extremely high sensitivities required to achieve the survey's primary science goals. Based on the distribution of 5σ limiting magnitudes in the F466N and F470N mosaics (in 0.3 arcsec diameter apertures), the limiting line fluxes are estimated to be $\sim 1.2 \times 10^{-18}$ erg s^{-1}cm^{-2} over 90 per cent of the field, reaching up to $\sim 2\times$ fainter emission lines than current slitless spectroscopic surveys in the literature. For the primary science goal of probing Hα at $z \sim 6.1$, these flux limits correspond to $\log_{10}(L_{\rm H\alpha}/{\rm erg\ s^{-1}}) \sim 41.53 - 41.76$, or unobscured SFRs of 0.9–1.3 M$_\odot$ yr^{-1}.

The F212N narrow-band mosaic reaches line sensitivities of 1.4–2.5×10^{-18} erg s^{-1}cm^{-2}, corresponding to $\log_{10}(L_{\rm H\alpha}/{\rm erg\ s^{-1}}) \sim$ 40.75–40.99; a factor of up to ~ 10 further down the $z = 2.23$ Hα LF than previously available from ground-based narrow-band surveys. The combination of this extraordinary depth with *JWST*'s exquisite spatial resolution offers an unprecedented view of the resolved star formation properties in galaxies at the peak of cosmic star formation history, for example by enabling detailed morphological comparison between Hα, UV and *in situ* stellar mass in representative samples of galaxies.

We have highlighted the unique science cases for the JELS observations: a census of Hα emitters at $z \sim 6.1$ that offers complementary constraints on the cosmic star formation history and the galaxy population in the early Universe, novel probes of both early (through [O III] emitters) and late stages (Hα at $z \sim 6.1$) of cosmic reionization, dust unbiased samples of star-forming galaxies at cosmic noon (Hα/Paα/Paβ), and spatially resolved properties of ionized gas in galaxies on sub-kpc scales at $2 \lesssim z \lesssim 6$. Through detailed simulations of realistic Hα and [O III]λ5008 emitter populations, we have also demonstrated that for intrinsic line luminosities above the JELS limiting magnitudes, the resulting photo-z estimates can be constrained to near spectroscopic accuracy ($\sigma_{\rm NMAD} < 0.005 \times (1 + z)$) for a wide range of intrinsic equivalent widths. These simulations also show that the emission-line luminosities estimated from the JELS narrow-band excess can be both extremely accurate (bias less than 0.01 dex) and measured with sufficient precision ($\pm0.05 - 0.1$dex) that the limiting precision on intrinsic properties will the precision to which dust attenuation corrections can be made (as is also the case in slitless spectroscopic surveys).

Initial results for the primary Hα sample at $z \sim 6.1$ and full JELS-selected photometry catalogues are presented in a companion paper, Pirie et al. (2025), with a number of further studies on the detailed properties of Hα, Paα/Paβ, and [O III] samples also in progress. With JELS adding both novel wavelength information (F212N, F466N, F470N) and significant additional broad-band sensitivity (F200W) within one of the key extra-galactic legacy fields, we expect the broader scientific return from the community to extend far beyond these initial goals.

ACKNOWLEDGEMENTS

We thank the anonymous referee for their helpful and constructive feedback that has significantly improved this manuscript. The authors also thank David Coulter and Armin Rest for allowing the inclusion of JELS targets in their director's discretionary observing programme. KJD acknowledges support from the Science and Technology Facilities Council (STFC) through an Ernest Rutherford Fellowship (grant number ST/W003120/1). DJM, PNB, RK, and RJM acknowledge the support of the UK STFC via grant ST/V000594/1. PNB and RK are grateful for support from the UK STFC via grant ST/Y000951/1. RKC was funded by support for programme #02321, provided by NASA through a grant from the Space Telescope Science Institute, which is operated by the Association of Universities for Research in Astronomy, Inc., under NASA contract NAS5-03127. RKC is grateful for support from the Leverhulme Trust via the Leverhulme Early Career Fellowship. JSD acknowledges the support of the Royal Society via a Royal Society Research Professorship. CLH acknowledges support from the Leverhulme Trust through an Early Career Research Fellowship and also acknowledge support from the Oxford Hintze Centre for Astrophysical Surveys which is funded through generous support from the Hintze Family Charitable Foundation. EI gratefully acknowledge financial support from ANID –MILENIO – NCN2024_112 and ANID FONDECYT Regular 1221846. AMS and IRS acknowledge support from the STFC via grant ST/X001075/1. This work was initiated in part at Aspen Center for Physics, which is supported by National Science Foundation grant PHY-2210452.

DATA AVAILABILITY

The data underlying this article are available in the Mikulski Archives for Space Telescopes (MAST) Portal under proposal ID numbers 2321 (JELS imaging) and 6585 (NIRSpec PRISM spectroscopy). Higher level data products, including all reduced mosaics in the JELS narrow and broad-band filters (v0.8 and v1.0), as well as associated catalogues presented in Pirie et al. (2025) are made available through the Edinburgh DataShare service. Any other data produced for the article will be shared on reasonable request to the corresponding author.

REFERENCES

Arellano-Córdova K. Z. et al., 2022, ApJ, 940, L23
Arrabal Haro P. et al., 2023, Nature, 622, 707

Bacon R. et al., 2010, in McLean I. S., Ramsay S. K., Takami H.,eds, Proc. SPIE Conf. Ser.Vol. 7735, Ground-based and Airborne Instrumentation for Astronomy III. SPIE, Bellingham, p. 773508
Baronchelli I. et al., 2020, ApJS, 249, 12
Begley R. et al., 2024, MNRAS, 527, 4040
Bhatawdekar R., Conselice C. J., Margalef-Bentabol B., Duncan K., 2019, MNRAS, 486, 3805
Bouwens R. J. et al., 2015, ApJ, 803, 34
Bouwens R. J., Illingworth G., Ellis R. S., Oesch P., Stefanon M., 2022, ApJ, 940, 55
Brammer G. B., van Dokkum P. G., Coppi P., 2008, ApJ, 686, 1503
Bunker A. J. et al., 2024, A&A, 690, A288
Byler N., Dalcanton J. J., Conroy C., Johnson B. D., 2017, ApJ, 840, 44
Calzetti D., Armus L., Bohlin R. C., Kinney A. L., Koornneef J., Storchi-Bergmann T., 2000, ApJ, 533, 682
Cameron A. J. et al., 2023, A&A, 677, A115
Carniani S. et al., 2017, A&A, 605, A42
Carniani S. et al., 2024, Nature, 633, 318
Cheng C. et al., 2020, MNRAS, 499, 5241
Clarke C., Oey M. S., 2002, MNRAS, 337, 1299
Cleri N. J. et al., 2022, ApJ, 929, 3
Cochrane R. K., Best P. N., Sobral D., Smail I., Wake D. A., Stott J. P., Geach J. E., 2017, MNRAS, 469, 2913
Cochrane R. K., Best P. N., Sobral D., Smail I., Geach J. E., Stott J. P., Wake D. A., 2018, MNRAS, 475, 3730
Cochrane R. K. et al., 2021, MNRAS, 503, 2622
Cochrane R. K. et al., 2023, MNRAS, 523, 2409
Conroy C., Gunn J. E., 2010, ApJ, 712, 833
Conroy C., Gunn J. E., White M., 2009, ApJ, 699, 486
Conselice C. J. et al., 2024, MNRAS, 531, 4857
Covelo-Paz A. et al., 2025, A&A, 694, A178
Curti M. et al., 2023, MNRAS, 518, 425
Curtis-Lake E. et al., 2023, Nat. Astron., 7, 622
De Barros S., Oesch P. A., Labbé I., Stefanon M., González V., Smit R., Bouwens R. J., Illingworth G. D., 2019, MNRAS, 489, 2355
de Graaff A. et al., 2025, A&A, 697, A189
Donnan C. T. et al., 2024, MNRAS, 533, 3222
Dudzevičiūtė U. et al., 2020, MNRAS, 494, 3828
Duncan K. J. et al., 2019, A&A, 622, A3
Endsley R., Stark D. P., Whitler L., Topping M. W., Chen Z., Plat A., Chisholm J., Charlot S., 2023, MNRAS, 524, 2312
Endsley R. et al., 2024, MNRAS, 533, 1111
Estrada-Carpenter V. et al., 2024, MNRAS, 532, 577
Ferland G. J. et al., 2013, RMxAA, 49, 137
Ferreira L. et al., 2022, ApJ, 938, L2
Flury S. R. et al., 2022, ApJ, 930, 126
Flury S. R. et al., 2025, ApJ, 985, 128
Gaia Collaboration, 2022, preprint (arXiv:2208.00211)
Geach J. E., Smail I., Best P. N., Kurk J., Casali M., Ivison R. J., Coppin K., 2008, MNRAS, 388, 1473
Geach J. E., Sobral D., Hickox R. C., Wake D. A., Smail I., Best P. N., Baugh C. M., Stott J. P., 2012, MNRAS, 426, 679
Greene J. E. et al., 2024, ApJ, 964, 39
Grogin N. A. et al., 2011, ApJS, 197, 35
Hao C.-N., Kennicutt R. C., Johnson B. D., Calzetti D., Dale D. A., Moustakas J., 2011, ApJ, 741, 124
Harikane Y. et al., 2022, ApJS, 259, 20
Hayes M., Schaerer D., Östlin G., 2010, A&A, 509, L5
Helton J. M. et al., 2024, ApJ, 962, 124
Hu W. et al., 2024, ApJ, 971, 21
Isobe Y. et al., 2023, ApJ, 959, 100
Jakobsen P. et al., 2022, A&A, 661, A80
Johnson B. et al., 2021a, dfm/python-fsps: python-fsps v0.4.1rc1, Zenodo, https://doi.org/10.5281/zenodo.4737461
Johnson B. D., Leja J., Conroy C., Speagle J. S., 2021b, ApJS, 254, 22
Kartaltepe J. S. et al., 2023, ApJ, 946, L15
Kashino D., Lilly S. J., Matthee J., Eilers A.-C., Mackenzie R., Bordoloi R., Simcoe R. A., 2023, ApJ, 950, 66
Khostovan A. A., Sobral D., Mobasher B., Smail I., Darvish B., Nayyeri H., Hemmati S., Stott J. P., 2016, MNRAS, 463, 2363
Killi M. et al., 2024, A&A, 691, A52
Koekemoer A. M. et al., 2011, ApJS, 197, 36
Labbe I. et al., 2025, ApJ, 978, 92
Larson R. L. et al., 2023a, ApJ, 953, L29
Larson R. L. et al., 2023b, ApJ, 958, 141
Le Fèvre O. et al., 2020, A&A, 643, A1
Liu Z., Morishita T., Kodama T., 2024, preprint (arXiv:2406.11188)
Madau P., Dickinson M., 2014, ARA&A, 52, 415
Maiolino R. et al., 2024, A&A, 691, A145
Mármol-Queraltó E., McLure R. J., Cullen F., Dunlop J. S., Fontana A., McLeod D. J., 2016, MNRAS, 460, 3587
Mascia S. et al., 2024, A&A, 685, A3
Maseda M. V. et al., 2023, ApJ, 956, 11
Maseda M. V. et al., 2024, A&A, 689, A73
Mason C. A., Treu T., Dijkstra M., Mesinger A., Trenti M., Pentericci L., de Barros S., Vanzella E., 2018, ApJ, 856, 2
Matharu J. et al., 2024, A&A, 690, A64
Matthee J., Sobral D., Best P., Smail I., Bian F., Darvish B., Röttgering H., Fan X., 2017, MNRAS, 471, 629
Matthee J., Mackenzie R., Simcoe R. A., Kashino D., Lilly S. J., Bordoloi R., Eilers A.-C., 2023, ApJ, 950, 67
Matthee J. et al., 2024, ApJ, 963, 129
Meyer R. A. et al., 2024, MNRAS, 535, 1067
Molina J., Ibar E., Smail I., Swinbank A. M., Villard E., Escala A., Sobral D., Hughes T. M., 2019, MNRAS, 487, 4856
Mortlock A. et al., 2013, MNRAS, 433, 1185
Muzzin A. et al., 2025, MINERVA: Unlocking the Hidden Gems of the Distant Universe and Completing HST and JWST?s Imaging Legacy with Medium Bands, JWST Proposal. Cycle 4, ID. #7814
Nelson E. J. et al., 2013, ApJ, 763, L16
Nelson E. J. et al., 2016, ApJ, 828, 27
Oesch P. A. et al., 2023, MNRAS, 525, 2864
Oke J. B., Gunn J. E., 1983, ApJ, 266, 713
Parsa S., Dunlop J. S., McLure R. J., Mortlock A., 2016, MNRAS, 456, 3194
Pirie C. A. et al., 2025, preprint (arXiv:2410.11808)
Pirzkal N. et al., 2018, ApJ, 868, 61
Pirzkal N. et al., 2024, ApJ, 969, 90
Prieto-Lyon G. et al., 2023, A&A, 672, A186
Reddy N. A. et al., 2018, ApJ, 869, 92
Reddy N. A., Topping M. W., Sanders R. L., Shapley A. E., Brammer G., 2023, ApJ, 952, 167
Rieke M. J., Kelly D., Horner S., 2005, in Heaney J. B., Burriesci L. G., eds, Proc. SPIE Conf. Ser.Vol. 5904, Cryogenic Optical Systems and Instruments XI. SPIE, Bellingham, p. 1
Rieke M. J. et al., 2023, PASP, 135, 028001
Rigby J. et al., 2023, PASP, 135, 048001
Robertson B. et al., 2024, ApJ, 970, 31
Robotham A. S. G., D'Silva J. C. J., Windhorst R. A., Jansen R. A., Summers J., Driver S. P., Wilmer C. N. A., Bellstedt S., 2023, PASP, 135, 085003
Roy N. et al., 2023, ApJ, 952, L14
Sanders R. L., Shapley A. E., Topping M. W., Reddy N. A., Brammer G. B., 2023, ApJ, 955, 54
Saxena A. et al., 2024, A&A, 684, A84
Scarlata C., Hayes M., Panagia N., Mehta V., Haardt F., Bagley M., 2024, preprint (arXiv:2404.09015)
Shapley A. E., Reddy N. A., Sanders R. L., Topping M. W., Brammer G. B., 2023, ApJ, 950, L1
Shen L. et al., 2024, ApJ, 963, L49
Simmonds C. et al., 2023, MNRAS, 523, 5468
Simmonds C. et al., 2024, MNRAS, 535, 2998
Smith A., Ma X., Bromm V., Finkelstein S. L., Hopkins P. F., Faucher-Giguère C.-A., Kereš D., 2018, MNRAS, 484, 39
Sobral D. et al., 2009, MNRAS, 398, 75
Sobral D., Best P. N., Geach J. E., Smail I., Cirasuolo M., Garn T., Dalton G. B., Kurk J., 2010, MNRAS, 404, 1551

Sobral D., Best P. N., Smail I., Geach J. E., Cirasuolo M., Garn T., Dalton G. B., 2011, MNRAS, 411, 675
Sobral D., Smail I., Best P. N., Geach J. E., Matsuda Y., Stott J. P., Cirasuolo M., Kurk J., 2013, MNRAS, 428, 1128
Sobral D., Kohn S. A., Best P. N., Smail I., Harrison C. M., Stott J., Calhau J., Matthee J., 2016, MNRAS, 457, 1739
Somerville R. S., Davé R., 2015, ARA&A, 53, 51
Stark D. P., Ellis R. S., Chiu K., Ouchi M., Bunker A., 2010, MNRAS, 408, 1628
Storey P. J., Hummer D. G., 1995, MNRAS, 272, 41
Storey P. J., Zeippen C. J., 2000, MNRAS, 312, 813
Stott J. P. et al., 2014, MNRAS, 443, 2695
Suess K. A. et al., 2024, ApJ, 976, 101
Sun G., Faucher-Giguère C.-A., Hayward C. C., Shen X., 2023a, MNRAS, 526, 2665
Sun G., Faucher-Giguère C.-A., Hayward C. C., Shen X., Wetzel A., Cochrane R. K., 2023b, ApJ, 955, L35
Swinbank M. et al., 2012, Messenger, 149, 40
Tang M. et al., 2023, MNRAS, 526, 1657
Tang M., Stark D. P., Topping M. W., Mason C., Ellis R. S., 2024, ApJ, 975, 208
Terao Y., Spitler L. R., Motohara K., Chen N., 2022, ApJ, 941, 70
Theios R. L., Steidel C. C., Strom A. L., Rudie G. C., Trainor R. F., Reddy N. A., 2019, ApJ, 871, 128
Topping M. W. et al., 2024, MNRAS, 529, 3301
Umeda H., Ouchi M., Nakajima K., Harikane Y., Ono Y., Xu Y., Isobe Y., Zhang Y., 2024, ApJ, 971, 124
Urrutia T. et al., 2019, A&A, 624, A141
Witstok J. et al., 2024, A&A, 682, A40
Wold I. G. B., Malhotra S., Rhoads J. E., Weaver J. R., Wang B., 2025, ApJ, 980, 200
Yung L. Y. A., Somerville R. S., Popping G., Finkelstein S. L., Ferguson H. C., Davé R., 2019, MNRAS, 490, 2855

APPENDIX A: JELS NARROW-BAND MOSAIC RELEASE VERSIONS

As outlined in Section 2, the initial JELS observations were impacted by severe scattered light. Initial versions of the JELS imaging products, including those used in Pirie et al. (2025, v0.8), made use of the data available and analysis pipelines at the time of analysis. The imaging products and associated depths presented in this manuscript correspond to the versions with all JELS observing programme (GO 2321) data acquired (v1.0). For completeness, here we outline the key differences in the JELS mosaic release versions and provide a quantitative comparison of the limiting emission-line sensitivities achieved by the respective versions. The key data and pipeline differences between images version are as follows:

(i) v0.8: Image reduction using PENCIL version based on *JWST* pipeline version 1.10.2 (JWST_1107.PMAP). Mosaics incorporate all frames observed 2023 May, with scattered light contribution subtracted from LW filters (F466N/F470N) and scattered light masked from impacted SW frames (F212N/F200W).

(ii) v1.0: Image reduction using PENCIL version based on *JWST* pipeline version 1.13.4 (JWST_1303.PMAP). Mosaics incorporate all frames observed 2023 May and 2024 November. Scattered light contributions subtracted from LW (F466N/F470N) and masked in SW (F212N/F200W) frames from 2023 May, with corresponding 2024 November frames included in addition.

In Fig. A1, we present the area per limiting sensitivity in each narrow-band filter for both v0.8 and v1.0 of the JELS mosaics following the procedure outlined in Section 2.3 (cf. Fig. 4). For F466N, where the scattered light impact was negligible and the input imaging for v0.8 and v1.0 is effectively unchanged, we find that the v1.0 mosaic achieves a consistent ~ 0.09 dex improvement in sensitivity across the full image; indicative of general NIRCam sensitivity improvements from revisions to the relevant read-noise and flat-field calibration files from the later CRDS version. For F470N, the sensitivity distribution includes the same ~ 0.09 dex systematic shift as for F466N, but with an additional increase in sensitivity from the repeat observations; a higher fraction of the mosaic is covered by two full visits at the full JELS exposure time, with an additional fraction now observed at $3\times \sim 6000$s.

For F212N, which was most severely impacted by the enhanced scattered light, the peak of the sensitivity distribution is ~ 0.2 dex fainter, reflecting the significantly increased area with $2\times \sim 6000$s visits (per the original survey design), a subset of area now with $3\times$ visits due to repeats, and similar systematic gains from calibration improvements. Based on the change in sensitivity of the shallowest regions of the field where no new data is included, we estimate that the systematic improvement in F212N sensitivity from CRDS reference file changes is smaller than for the LW bands, at the level of ~ 0.05 dex.

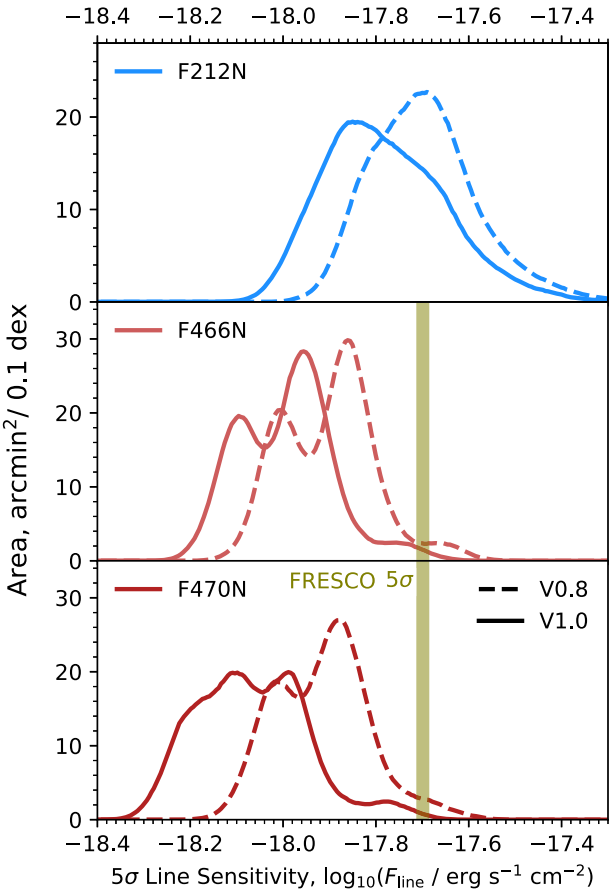

Figure A1. Emission-line sensitivity of the JELS narrow-bands as a function of area per limiting sensitivity for v0.8 of the JELS mosaics (e.g. Pirie et al. 2025, dashed lines) and the v1.0 mosaics presented here (solid lines). Also plotted for reference for the F466N and F470N panels is the average 5σ limiting line sensitivity for the FRESCO slitless spectroscopy survey (thick vertical line; Oesch et al. 2023).

For all three JELS narrow-band filters, we note that while the gains in sensitivity for v1.0 are consistent and statistically significant with respect to our ability to constrain the image noise itself, the changes are not as scientifically significant. Impacts to the robust emission-line samples produced from JELS imaging and the predictions of the simulations presented in Section 4 are negligible between versions. Sample sizes from v1.0 may be increased in size, but only at the 10–20 per cent level. However, the inferred properties and redshifts for individual objects are as robust in v0.8 as in v1.0 due to the more significant impacts of large photometric uncertainties in other filters for sources near the detection limit and the standard inclusion of 5–10 per cent flux uncertainties for photo-z/SED-fitting analysis.

APPENDIX B: CORRECTING FOR [O III]λ4960 CONTRIBUTIONS IN [O III]λ5008 LUMINOSITY ESTIMATION

For the [O III]λ5008 emission-line selection, the JELS narrow-bands are sufficiently narrow that typically only one of the [O III] doublet lines contributes the majority of flux at any given redshift (unlike for some lower redshift narrow-band surveys where both [O III] line, and sometimes Hβ, are often encompassed by the narrow-band filter, e.g. Khostovan et al. 2016). The contribution from the secondary line, i.e. [O III]λ4960 for [O III]λ5008 excess selection, however, is non-negligible and naive estimates of the line flux based on the narrow-band colour excess alone could therefore overestimate the true [O III]λ5008 line flux. Furthermore, given the high-EWs of the $z \sim 8.3$ samples, the [O III]λ4960 emission will have significant contribution to the surrounding broad-band flux, $f_{\lambda,\mathrm{F444W}}$, that could lead to an overestimate of the stellar continuum level and hence an underestimate of the inferred [O III]λ5008 flux. Formally, high-EW Hβ emission will also contribute to an overestimate of the stellar continuum, however given the high [O III]/Hβ ratios observed at $z > 6$ (Sanders et al. 2023; Shapley et al. 2023), we assume that any resulting corrections would be negligible relative to the photometric uncertainties. Regardless, the relative balance of these two competing secondary or tertiary line contaminations will depend on the precise redshift. We therefore implement a simple analytic correction based on the expected relative contribution of the [O III] lines to both the narrow-band and broad-band filter fluxes. For the simplifying assumption that the emission lines themselves have effectively no velocity dispersion, and assuming the standard ratio of [O III]λ5008/[O III]λ4960 = 2.98, the relative contributions of both [O III] lines to a given filter, $f_{\mathrm{OIII},i}$, is proportional to

$$f_{\mathrm{OIII},i} \propto f_{\lambda5008}\tilde{t}_{i,\lambda5008}(z) + \frac{f_{\lambda5008}}{2.98}\tilde{t}_{i,\lambda4960}(z), \quad \text{or}$$
$$f_{\mathrm{OIII},i} \propto f_{\lambda5008}\left(\tilde{t}_{i,\lambda5008}(z) + \frac{\tilde{t}_{i,\lambda4960}(z)}{2.98}\right), \tag{B1}$$

where $\tilde{t}_{i,\mathrm{line}}(z)$ is the filter throughput at the wavelength of the corresponding line at redshift z, normalized to the peak filter throughput. The redshift-dependent correction factor, $C_i(z)$, to relate the observed flux to that corresponding to only the [O III]λ5008 flux can then simply be defined as

$$C_i(z) = \frac{1}{\tilde{t}_{i,\lambda5008}(z) + \frac{\tilde{t}_{i,\lambda4960}(z)}{2.98}}. \tag{B2}$$

Equation (2) can then be modified such that the [O III]λ5008 emission-line flux can estimated as

$$F_{\lambda5008}(z) = \Delta\lambda_{\mathrm{F466N}}\,\frac{f_{\lambda,\mathrm{F466N}}C_{\mathrm{F466N}}(z)\; f_{\lambda,\mathrm{F444W}}C_{\mathrm{F444W}}(z)}{1\,(\Delta\lambda_{\mathrm{F466N}}/\Delta\lambda_{\mathrm{F444W}})}$$
$$\mathrm{erg\ s^{-1}cm^{-2}}. \tag{B3}$$

From tests convolving model [O III] emission lines with the F466N and F444W filters over a range of plausible velocity dispersions and across the redshift range probed by the excess selection, we find that the simplifying assumption of infinitely narrow intrinsic lines is accurate to ~ 1 per cent for intrinsic velocity dispersions with FWHM less than 250 km s^{-1}. When estimating the line luminosity for an [O III]λ5008 source, we then draw 100 redshifts from the photo-z posterior, calculating $F_{\lambda5008}(z)$ using equation (B3) and incorporating the redshift into the corresponding luminosity distance calculation. The estimated line luminosity for an individual source including the uncertainty from the redshift-dependent [O III]λ4960 contribution can then be derived from the resulting distribution (i.e. 16, 50, and 84th percentiles).

This paper has been typeset from a TEX/LATEX file prepared by the author.

© The Author(s) 2025.
Published by Oxford University Press on behalf of the American Institute of Biological Sciences. This is an Open Access article distributed under the terms of the Creative Commons Attribution License (https://creativecommons.org/licenses/by/4.0/), which permits unrestricted reuse, distribution, and reproduction in any medium, provided the original work is properly cited.